Renal Coenzyme A (CoA) Production Fuels Stem Cell Proliferation and Tumor Growth

Ting Miao[1,^], Ying Liu[1], Mujeeb Qadiri[1], John M Asara[2], Yanhui Hu[1], Xiaomei Sun[1], Christian Dibble[3^], Norbert Perrimon[1,4,^]

[1] Department of Genetics, Blavatnik Institute, Harvard Medical School, Boston, MA, USA.

[2] Mass Spectrometry Core, Beth Israel Deaconess Medical Center and Department of Medicine, Harvard Medical School, Boston, MA USA

[3] Department of Pathology, Cancer Research Institute, Beth Israel Deaconess Medical Center, Harvard Medical School, Boston, MA, USA

[4] Howard Hughes Medical Institute, Boston, MA, USA

^Correspondence:

Ting Miao: ting_miao@hms.harvard.edu

Norbert Perrimon: perrimon@genetics.med.harvard.edu

Christian Dibble: ccdibble@bidmc.harvard.edu

Abstract

Coenzyme A (CoA), derived from Vitamin B5 (VB5), is essential for lipid metabolism, energy production, and cell proliferation. While the intracellular functions of CoA are well characterized, its tissue-specific regulation and systemic physiological roles remain poorly understood. Here, using *Drosophila melanogaster*, we uncover a gut-renal circuit in which dietary VB5 stimulates CoA biosynthesis specifically in the Malpighian tubules (MTs, the fly kidney), non-autonomously impacting gut homeostasis. We show that Myc boosts renal CoA production by directly upregulating *Fbl* (*PANK1-3* homolog) and downregulating *dPANK4* in the MTs. Elevated CoA biosynthesis enhances the mevalonate-isoprenoid pathway activity in the gut, promoting intestinal stem cell proliferation. We further demonstrate that renal CoA production is required for gut tumor growth in a fly model. Consistently, *MYC* and genes within the CoA-isoprenoid axis display strong association with clinical outcomes in human cancers. Together, our findings establish that Myc-driven CoA metabolism generates an inter-organ signal that couples VB5 availability to stem cell control and tumor growth, and identify the CoA-isoprenoid axis as a targetable metabolic vulnerability in cancer.

Introduction

Dietary supplementation with B vitamins is a common practice worldwide [1], valued for their beneficial roles in fundamental biological processes such as energy production, nervous system function, and immune responses [2, 3]. While all B vitamins function as critical cofactors or cofactor precursors in central metabolism, their dietary effects are not uniformly advantageous. Under certain conditions, they can produce unexpected and even adverse outcomes, for example, promoting leukemic cell proliferation [4]. These findings underscore that our understanding of B vitamin metabolism in physiological and pathological states remains incomplete.

A particularly important member of this family is Vitamin B5 (VB5), or pantothenic acid, the nutrient precursor of Coenzyme A (CoA) in mammals [5]. CoA is a central metabolic cofactor required for over 100 enzymatic reactions, including the tricarboxylic acid (TCA) cycle, fatty acid β-oxidation, amino acid catabolism, and lipid and sterol synthesis [5-8]. In either mammals or insects, VB5 cannot be *de novo* synthesized and is largely obtained from the diet. It is then absorbed in the intestine and transported into cells via SLC5A6/SMVT, enabling CoA biosynthesis across diverse tissues [7, 8]. CoA is synthesized *de novo* from VB5 via a conserved five-step enzymatic pathway, initiated by the phosphorylation of VB5 by pantothenate kinases (PANK1-3) [7]. Notably, we recently identified PANK4, a pseudo-pantothenate kinase, as a rate-determining enzyme and negative regulator of CoA biosynthesis in mammalian cells [9]. The pantothenate kinase activity of mammalian PANK1-3 (and of PANKs in other species including most bacteria) is modulated by direct feedback inhibition from CoA and acyl-CoAs [10, 11], and responds to nutrient signals such as insulin via post-translational modifications, including PI3K/Akt-mediated phosphorylation of PANK2 and PANK4 [9]. Transcriptional control is another important regulatory layer, but only a limited number of transcription factors have so far been uncovered that regulate genes involved in CoA transport or biosynthesis. For example, PANK1 is a direct transcriptional target of the tumor suppressor and transcription factor p53 [12, 13], while the oncogene MYC has been shown to regulates CoA biosynthesis by driving the expression of VB5 transporter SLC5A6/SMVT [14, 15]. Whether MYC also directly regulates CoA biosynthetic enzymes to control CoA production remains unknown. Notably, total CoA levels differ by more than 10-fold across mammalian tissues [7], suggesting that CoA metabolism is highly tissue-specific and coordinated across tissues. However, the mechanisms underlying tissue-specific CoA metabolic regulation remains poorly defined, limiting our understanding of how CoA metabolism is tuned across organs in response to physiological and pathological cues. This is particularly important in high-metabolic-turnover organs such as the kidney, which exhibits high CoA levels [7, 8] but whose regulatory networks governing CoA metabolism remain poorly understudied.

CoA availability is essential for lipid metabolism, particularly fatty acid (FA) and mevalonate (MVA) biosynthesis [16, 17]. FA synthesis begins with acetyl-CoA and malonyl-CoA and yields diverse lipids for membranes and energy storage [16, 18]. The MVA pathway, initiates with a multi-step conversion of acetyl-CoA to 3-hydroxy-3-methylglutaryl-CoA (HMG)-CoA, is essential in multiple cancer cell types [19-22]. Pharmacological inhibition of this pathway by targeting the rate-limiting enzyme HMG-CoA reductase (HMGCR) with statins reduces tumor growth and promotes apoptosis, underscoring the dependency of tumors on MVA pathway activity [19-22]. A major output of the MVA pathway is the synthesis of isoprenoid backbones, catalyzed by the key enzymes such as farnesyl diphosphate synthase (FDPS) and geranylgeranyl diphosphate synthase 1 (GGPS1). These backbones serve as precursors for a range of downstream metabolic products, including ubiquinone (CoQ), dolichol, sterols, and prenylation substrates [17]. While much focus has been placed on cholesterol as the major tumor-promoting metabolite [23], emerging evidence suggests that non-sterol isoprenoids also influence cancer cell behavior. For example, the availability of geranylgeranyl pyrophosphate (GGPP), a key isoprenoid intermediate mediating protein prenylation, has been shown to promotes cancer cell proliferation [24, 25]. Nevertheless, although other isoprenoid-derived metabolites are known to participate in key cellular processes such as cell cycle progression and mitochondrial function [17, 26], their specific contributions to tumor growth and survival remain largely undefined.

Drosophila is a powerful model organism for investigating tissue homeostasis, metabolism, and inter-organ communication [27, 28]. Importantly, flies share conserved VB5-CoA biosynthetic pathways with mammals and possess tissue analogs to major human organs, making it an ideal system for studying tissue-specific CoA metabolism. In this study, we investigated how VB5-CoA metabolism influences gut tissue homeostasis and tumor growth in flies. We show that dietary VB5 supplementation or renal-specific activation of CoA biosynthesis is sufficient to drive intestinal stem cell (ISC) proliferation via enhanced MVA-isoprenoid pathway in the gut. In addition, we identify Myc as a direct transcriptional regulator of this pathway. In a Yorkie/Yki-driven fly gut tumor model [29], tumor-derived PDGF/VEGF signaling upregulates *Myc* in renal cells, which in turn drives CoA biosynthesis to support tumor growth. Importantly, we demonstrate the clinical relevance of MYC-driven CoA-isoprenoid axis in human cancer progression, identify CoA-isoprenoid pathway as a potential therapeutic target in kidney cancer. Together, our work establishes a functional inter-organ circuit of CoA metabolism, with broad implications for understanding systemic metabolic regulation and developing therapeutic interventions in cancer.

Results

VB5 supplementation stimulates intestinal stem cell ISC proliferation

While the B vitamins are essential for systemic health [2, 3], its specific roles in regulating tissue homeostasis remain poorly characterized. To investigate this, we employed the *Drosophila* midgut, a highly plastic organ that serves as an ideal model for dissecting the nutritional and metabolic control of tissue homeostasis [30-32]. We supplemented fly diets with major B vitamins individually, including thiamine (VB1), riboflavin (VB2), niacin (VB3), pantothenate (VB5), pyridoxine (VB6), and biotin (VB7) **(Fig. 1a)**. Notably, VB5 supplementation led to significant expansion of the midgut, reflected by increased width in the R4-R5 regions **(Fig. 1b-c)**, suggesting a role of VB5 in maintaining midgut homeostasis. Since *Drosophila* midgut homeostasis is maintained by proliferating intestinal stem cells (ISCs) [30, 31], we assessed the ISC proliferation under these conditions through staining for phospho-Histone 3 (pH3), a marker of mitotic activity [30, 31]. Consistent with the observed midgut expansion, VB5-fed flies exhibited a significant increase in pH3-positive ($pH3^+$) ISCs compared to controls **(Fig. 1b, d)**, suggesting enhanced ISC proliferation. We further validated this phenotype by supplementing fly diets with a range of VB5 concentrations. Interestingly, we observed a modest increase in $pH3^+$ signal with 1 mM VB5 supplementation and a more pronounced effect at 2.5 mM **(Fig. 1e)**, indicating a linear and dose-dependent response to dietary VB5 supplementation.

ISCs maintain midgut homeostasis through differentiating into progenitor state enteroblasts (EBs), which then terminally differentiate into enterocytes (ECs) or enteroendocrine cells (EEs), respectively [32] **(Fig. 1a)**. To further investigate how VB5 affects gut tissue homeostasis, we followed the percentage of gut cell subtypes by using cell type-specific Gal4 drivers to express GFP: EGT-Gal4 (ISC/EB), Su(H)-GBE-Gal4 (EB), and Myo1A-Gal4 (EC) **(Fig. 1f-h)**. Notably, VB5 supplementation increased the number of ISCs and EBs, suggesting an elevated proportion of EBs resulted from ISC division. Together, our data indicates that dietary VB5 induces midgut expansion by stimulating ISC proliferation, uncovering a previously unappreciated role for VB5 in modulating intestinal tissue homeostasis.

CoA biosynthesis in the Malpighian tubules (MTs) non-autonomously regulates ISC proliferation

VB5 serves as a precursor in the *de novo* biosynthesis of CoA, an essential molecule in numerous fundamental biological processes [5-7]. The CoA biosynthetic pathway is highly conserved across species and known regulatory inputs primarily control the function of the PANK1-3 and PANK4 [7, 9] **(Fig. 2a)**. In *Drosophila*, the single pantothenate kinase orthologous to PANK1-3 is encoded by the gene *Fumble* (*Fbl*) [33] while an ortholog for PANK4 has not been previously characterized in flies. Here, based on sequence

alignments and functional characterization, we identify the previously uncharacterized protein CG5828 as the specific orthologue of mammalian PANK4's phosphatase domain. **(Fig. 2b and Extended Data Fig. 1a)**. Accordingly, we designate CG5828 as *Drosophila* PANK4 (dPANK4).

To determine whether the gut CoA biosynthetic pathway contributes to the VB5-induced ISC proliferation, we first assessed the expression of *Fbl* and *dPANK4* in the gut following dietary VB5 supplementation and found that their transcript levels remained unchanged **(Fig. 2c)**. Next, we knocked down *Fbl* in the gut using the temperature-sensitive EGT-Gal4 driver (hereafter referred to as Gut^{ts}>). However, *Fbl* knockdown did not suppress VB5-induced ISC proliferation **(Extended Data Fig. 1b)**. These results suggest that CoA biosynthesis in the gut may not be required for VB5-induced ISC proliferation.

To determine whether CoA biosynthesis in another tissue mediates VB5-induced ISC proliferation in a non-autonomous manner, we examined the expression pattern of CoA biosynthetic genes using FlyCellAltas [34], a reference single-cell transcriptomic database profiling gene expression dynamics across *Drosophila* tissues. Although *Fbl* expression is enriched broadly across various tissues, including fat body, oenocytes, heart, gut, and Malpighian tubules (MTs; functionally analogous to human kidney), *dPANK4* expression is predominantly enriched in MTs, particularly in principal cells (**Extended Data Fig. 1c-d)** [35]. Since PANK4 acts as a negative regulator of CoA biosynthesis, the relatively high *dPANK4* expression in the MTs suggests that this tissue may harbor a high intrinsic capacity for CoA biosynthesis that is restrained under certain physiological conditions. Supporting this hypothesis, VB5 supplementation significantly downregulated *dPANK4* and upregulated *Fbl* expression in the MTs **(Fig. 2d)**, suggesting increased CoA biosynthesis in this tissue. To test whether MT-specific CoA biosynthesis influences ISC proliferation, we knocked down *dPANK4* using the temperature-sensitive, MT principal cell-specific driver (hereafter referred to as MT^{ts}>) [36]. Indeed, *dPANK4* knockdown in the MTs led to more than fivefold increase in ISC proliferation, as indicated by $pH3^{+}$ cell counts **(Fig. 2e-f and Extended Data Fig. 1e)**. This effect was consistently observed in both female and male flies **(Extended Data Fig. 1f)** and validated using two additional independent RNAi lines **(Extended Data Fig. 1g)**. Importantly, the ISC proliferation phenotype was dependent on VB5 availability, as MT^{ts}>$dPANK4^{RNAi}$ flies fed on a VB5-deprived diet did not exhibit increased ISC proliferation **(Fig. 2g)**. Together, our data suggests that dietary VB5 supplementation activates CoA biosynthesis in the MTs, which in turn non-autonomously drives ISC proliferation in the gut.

Building on these findings, we hypothesized that CoA biosynthesis in the MT may be activated under specific physiological conditions to support gut homeostasis and renewal. To test this, we examined the effects of mating, a well-established physiological stimulus known to induce ISC proliferation in female flies [37, 38]. Intriguingly, mating significantly downregulated the expression of *dPANK4* in the MTs **(Fig. 2h)**, suggesting that mating

promotes CoA production by relieving dPANK4-mediated inhibition. Supporting this, overexpression of *dPANK4* in the MTs, which suppresses CoA production, completely abolished mating-induced ISC proliferation **(Fig. 2i and Extended Data Fig. 1h-i)**. Altogether, these data indicate that CoA biosynthesis in MTs is required to maintain gut homeostasis and renewal in response to both dietary VB5 supplementation and physiological stimulation.

To further access the systemic impact of MT CoA biosynthesis, we performed targeted liquid chromatography-coupled tandem mass spectrometry (LC-MS/MS) based metabolomics analyses on whole-body samples from flies with and without MT-specific *dPANK4* knockdown. Importantly, pathway enrichment analysis identified VB5 and CoA biosynthesis as the most significantly affected metabolic pathway **(Fig. 2j)**. Consistently, VB5 levels were significantly reduced in *dPANK4* knockdown flies **(Extended Data Fig. 1i)**, suggesting altered CoA synthesis. To directly measure CoA biosynthetic flux, we fed flies with heavy isotope($^{13}C_3{}^{15}N_1$)-labeled VB5 and performed LC-MS/MS-based isotopic tracing metabolomics to monitor the incorporation of labeled VB5 into CoA and its derivatives. Notably, we observed a significant increase in the fractional abundance of labeled CoASH (unesterified CoA) and several key acyl-CoAs including acetyl-CoA, malonyl-CoA, and HMG-CoA in whole MT^{ts}>$dPANK4^{RNAi}$ flies **(Fig. 2k)**, indicating a conserved role of dPANK4 in suppressing *de novo* CoA biosynthesis. Moreover, there were also elevated labeled fractions of CoA derivatives, including acetyl-CoA, malonyl-CoA, and HMG-CoA **(Fig. 2k)**. These findings reveal that MT-derived CoA contributes to the systemic CoA and acyl-CoA pools, implicating the renal system as a central site for CoA production in flies. Collectively, our results demonstrate that VB5 supplementation or physiological stimuli can activate CoA biosynthesis specifically in the MTs, which in turn promotes ISC proliferation in the gut. Our findings identify dPANK4 as a key regulator of CoA biosynthesis *in vivo* and highlight the MT as a central source of systemic CoA, linking renal CoA production to whole-body metabolic coordination and gut homeostasis.

MT CoA production promotes gut MVA and isoprenoid backbone biosynthesis

CoA is a central cofactor involved in numerous cellular processes, including *de novo* lipogenesis and protein acetylation, through the function of its key derivative, acetyl-CoA [16, 18, 39]. We therefore investigated whether activation of CoA production in the MTs influences gut homeostasis by altering these downstream pathways. We first measured the expression of essential lipogenic genes in the gut of MT^{ts}>$dPANK4^{RNAi}$ flies. However, transcription levels of *Acly* (ATP citrate lyase), *AcCoAS* (acetyl-CoA synthetase), *Acc* (acetyl-CoA carboxylase), and *FASN1* (fatty acid synthase 1) were unchanged **(Extended Data Fig. 2a)**. Consistent with this, BODIPY lipid staining showed no increase in lipid droplet accumulation in the gut of MT^{ts}>$dPANK4^{RNAi}$ flies **(Extended Data Fig. 2b-c)**.

These observations suggest that lipid synthesis may not be activated in the gut upon increased CoA biosynthesis in the MTs. We next examined protein acetylation, a post-translational modification derived from acetyl-CoA that modulates a wide range of cellular functions [39]. Protein acetylation is catalyzed by lysine acetyltransferases (KATs), which transfer acetyl groups from acetyl-CoA to lysine residues on target proteins [40]. Although we observed increased expression of several KAT homologs in the guts of *MT^{ts}>dPANK4^{RNAi}* flies, including *Mof* (*KAT8*), *Hat1*, and *Gcn5* **(Extended Data Fig. 2d)**, knocking down these genes in the gut did not block VB5-induced ISC proliferation **(Extended Data Fig. 2e)**, suggesting that protein acetylation is unlikely to be the primary driver of this response.

To further investigate how CoA biosynthesis in the MTs influences gut homeostasis, we performed targeted metabolomics on gut samples from MT specific *dPANK4*-knockdown flies. Pathway enrichment analysis identified several impacted metabolic pathways, including thiamine metabolism, arginine and proline metabolism, and isoprenoid backbone biosynthesis **(Fig. 3a)**. Intriguingly, our heavy isotope-labeled VB5 tracing and metabolomics analysis revealed that *dPANK4* knockdown enhanced labeled VB5 incorporation into HMG-CoA **(Fig. 2k)**, indicating that HMG-CoA biosynthesis was promoted. Given that HMG-CoA is primarily used for MVA production [22], the key entry point for isoprenoid backbone synthesis **(Fig. 3b)**, we hypothesized that these pathways may be activated in the gut in response to enhanced CoA production in the MTs. To test this hypothesis, we examined the expression of genes encoding key enzymes in the MVA and isoprenoid backbone biosynthesis pathways, including *Hmgcr*, *Fpps* (fly homolog of *FDPS*), and *Qm* (*Quemao*, fly homolog of *GGPS1*). Indeed, all three genes were upregulated in the guts of *MT^{ts}>dPANK4^{RNAi}* flies **(Fig. 3c)**. Additionally, the expression of *β-GGT-I* (β subunit of type I geranylgeranyl transferase, fly homolog of *PGGT1B*), an enzyme mediating protein prenylation utilizing GGPP derived from isoprenoid backbone biosynthesis pathway, was also elevated **(Fig. 3c)**. These results suggest that the MVA and isoprenoid backbone biosynthesis is activated in the gut in response to increased CoA biosynthesis in the MTs. To test whether MVA pathway acts downstream of MT CoA biosynthesis to drive ISC proliferation, we fed flies with or without MT-specific *dPANK4* depletion a diet supplemented with simvastatin, a well-established MVA pathway inhibitor **(Fig. 3b)** [41]. Supporting our hypothesis, simvastatin treatment significantly suppressed the increased pH3^{+} signal in the gut of *MT^{ts}>dPANK4^{RNAi}* flies **(Fig. 3d and Extended Data Fig. 2f)**, suggesting that MVA pathway activity is required for ISC proliferation induced by CoA biosynthesis in the MTs. To further validate this, we genetically disrupted the MVA and isoprenoid biosynthesis pathways in the gut by knocking down *Hmgcr* or *qm* and assessed ISC proliferation in response to VB5 supplementation. Intriguingly, the results showed that VB5-induced ISC proliferation was completely blocked by knockdown of either gene **(Fig. 3e)**, demonstrating that both MVA and isoprenoid backbone biosynthesis in the gut are essential for this effect. We next explored the downstream

mechanisms of MVA-isoprenoid pathway activity. Although cholesterol biosynthesis is a well-characterized output of the MVA-isoprenoid pathway implicated in cell proliferation and tumor progression in mammals, this branch is absent in insects [23, 42]. We therefore tested for effects on protein prenylation which relies on isoprenoid intermediates and is mediated by *β-GGT-I*, a known regulator of cell proliferation and organ overgrowth in *Drosophila* [43]. Consistently, gut-specific knockdown of *β-GGT-I* completely abolished VB5-induced ISC proliferation **(Fig. 3e)**. Collectively, these results demonstrate that MT-derived CoA pool influences gut homeostasis through the MVA-isoprenoid biosynthesis pathway.

A remaining question is how activation of the MVA-isoprenoid pathways in the gut is mechanistically coupled to CoA biosynthesis in the MT. Since CoA itself is not transported across the plasma membrane [5], we considered the possibility that CoA-derived metabolites are transported from the MT to the gut, where they activate MVA-isoprenoid biosynthesis and promote ISC proliferation. While inter-organ metabolite exchange often occurs via the circulatory system (hemolymph in *Drosophila*), the MTs and gut are anatomically connected **(Fig. 1a)**, raising the possibility of direct metabolite transfer via the shared lumen. Supporting this, we observed a spatially patterned increase in $pH3^+$ cells in the midgut of flies with MT-specific knockdown of *dPANK4*. These mitotic signals first appeared in the posterior R4-R5 region, which lies adjacent to the MT-gut junction, and progressively spread anteriorly upon prolonged *dPANK4* knockdown **(Fig. 1a and Extended Data Fig. 2g)**. This spatially restricted onset of proliferation and non-uniform distribution of mitotic cells suggest that the pro-proliferative signal may be locally transferred from the MTs to the gut, rather than disseminated through the hemolymph. A recent study reported that direct fluid exchange between the MTs and gut in *Drosophila* is mediated by aquaporins such as Drip [44]. *Drip* is expressed in both stellate cells and principal cells of the MTs **(Extended Data Fig. 2h)** where it facilitates water flux through the renal tubules [35, 45]. To determine whether aquaporin-mediated water flux is involved in the inter-organ metabolite exchange, we knocked down *Drip* in stellate cells (tsh^{ts}>) or in principal cells (MT^{ts}>). Consistent with the observation that *dPANK4* is enriched in principal cells **(Extended Data Fig. 1d)**, *Drip* knockdown in this cell type completely abolished VB5-induced ISC proliferation **(Fig. 3f)**. In contrast, knockdown of *Drip* in stellate cells had no effect **(Extended Data Fig. 2i)**. Altogether, these results suggest that CoA-derived metabolites access the gut from the MTs via aquaporin-mediated water influx, where they activate the MVA and isoprenoid backbone biosynthesis pathways to promote ISC proliferation.

MT CoA biosynthesis promotes gut tumor growth

Local CoA biosynthesis has been implicated in oncogenic metabolism and tumor progression [9, 15], yet the role of host CoA metabolism to tumor growth via inter-organ metabolite exchange remains unexplored. To investigate this, we employed a *Drosophila* gut tumor model driven by overexpression of a constitutively active form of the transcriptional co-activator and Hippo pathway effector, *Yorkie* ($yki^{[S3A]}$), in the ISCs (hereafter referred to as Yki flies) [29, 46]. We observed significant transcriptional changes in CoA biosynthesis genes, *Fbl* and *dPANK4*, specifically in the MT principal cells, but not in the gut ISCs/tumors **(Fig. 4a and Extended Data Fig. 3a)**, suggesting a potential contribution of MT-derived CoA synthesis to gut tumor growth. Supporting this, our previous full-body single-nucleus RNA-seq (snRNA-seq) analysis of Yki flies revealed elevated expression of the VB5 transporter *Smvt* that is known to stimulate CoA biosynthesis [15], in the MT principal cells but not in ISCs **(Extended Data Fig. 3a)** [46]. This observation suggests that dietary VB5 is preferentially transported to the MTs for CoA production in the Yki model. To decipher the role of MT CoA biosynthesis in gut tumor growth, we used a dual binary expression system (UAS-Gal4 and LexAop-LexA) to simultaneously induce tumor in the gut and knock down *Smvt* in the MTs ($Gut^{ts}>yki^{[S3A]}$, $MT^{ts}>Smvt^{RNAi}$). Interestingly, *Smvt* knockdown in the MTs significantly suppressed tumor growth in Yki flies **(Fig. 4b)**. Further, we inhibited MT CoA biosynthesis through either knocking down the biosynthetic enzyme *Fbl* or overexpressing the negative regulator *dPANK4* in Yki flies ($Gut^{ts}>yki^{[S3A]}$, $MT^{ts}>Fbl^{RNAi}$ and $Gut^{ts}>yki^{[S3A]}$, $MT^{ts}>dPANK4$). Both interventions significantly suppressed tumor growth, as evidenced by reduced gut width, decreased Yki-GFP signal, and lower mitotic ($pH3^{+}$) cell counts **(Fig. 4c-f and Extended Data Fig. 3b-i)**. Consistent with reduced tumor burden, inhibition of CoA biosynthesis in the MTs also ameliorated the bloating phenotype of Yki flies, a symptom of systematic fluid imbalance **(Fig. 4c, g-h and Extended Data Fig. 3f, j)** [29], and extended their overall survival **(Fig. 4i)**. These findings indicate that MT CoA biosynthesis promotes tumor growth and contributes to systemic disease progression in this model.

We have demonstrated that MVA-isoprenoid axis functions downstream of MT CoA biosynthesis to promote ISC proliferation in the wild-type flies **(Fig. 3)**. We next asked whether tumor cell proliferation is similarly driven by the activation of the MVA-isoprenoid biosynthetic pathway. Supporting this hypothesis, we observed upregulation of key genes involved in these pathways, including *Hmgcr*, *Fpps*, *Qm*, and *β-GGT-I*, in the gut tumors **(Fig. 4j)**. Consistent with this transcriptional activation, targeted metabolomics analysis of the gut samples from Yki flies revealed significant enrichment of the isoprenoid backbone biosynthesis pathway **(Extended Data Fig. 3k)**, along with notable accumulation of intermediate metabolites, including MVA, geranyl pyrophosphate (GPP), and farnesyl pyrophosphate (FPP) **(Fig. 4k)**, suggesting robust activation of the MVA-isoprenoid axis in the gut tumor. To further test whether MVA pathway activity is functionally required for tumor growth, we treated Yki flies with simvastatin, a specific inhibitor of MVA pathway. Consistent with our hypothesis, simvastatin treatment

significantly reduced tumor cell proliferation **(Fig. 4l)** and ameliorated the associated bloating phenotype **(Fig. 4m and Extended Data Fig. 3l)**. In summary, the results demonstrate that CoA biosynthesis is upregulated in the MTs of tumor-bearing flies and is required for intestinal tumor growth. Enhanced CoA production in the MTs correlates with activation of the MVA-isoprenoid axis in the gut which supports tumor cell proliferation, suggesting an inter-organ communication mechanism similar to that observed in wild-type flies. More broadly, these findings provide evidence for an MT/kidney-gut metabolite exchange as a shared regulatory mechanism underlying both gut tissue homeostasis and tumor growth.

Myc transcriptionally regulates CoA biosynthesis genes in the MTs

We previously reported that the PI3K-AKT signaling axis regulates CoA synthesis through phosphorylation of PANK4 in mammalian cells [9]. However, the *Drosophila* PANK4 ortholog, dPANK4, lacks the conserved phosphorylation sites found in mammalian PANK4 **(Fig. 2b).** Nevertheless, our data indicate that dPANK4 transcript levels are altered by several physiological and pathological conditions in *Drosophila* **(Fig. 2b, 2h, 4a)**, suggesting that *dPANK4* may be subject to transcriptional rather than post-translational regulation. To identify transcriptional regulators of CoA biosynthesis, we employed the Transcription Factor-to-Target Gene (TF2TG) prediction tool [47] to analyze the promoter and intron regions (up to 1.5 kb upstream) of six *Drosophila* CoA biosynthetic genes **(Fig. 2a)**. This analysis identified 250 candidate transcription factors (TFs). Among them, six TFs, including the well-characterized oncogenic factor Myc, were predicted to regulate all six genes **(Extended Data Table2)**. Notably, MYC has previously been linked to CoA metabolism in mammals through its regulation of the VB5 transporter SLC5A6/SMVT [15]. We have shown that CoA biosynthesis pathway is upregulated in the MTs of Yki flies at transcriptional level **(Fig. 4a and Extended Data Fig. 3a)**. Consistently, TF regulon analysis of our published Yki snRNA-seq data [46] identified Myc as the most significantly activated TF in the MTs of Yki flies **(Extended Data Fig. 4a).** These findings suggest that Myc may modulate CoA biosynthesis gene expression in the MTs. Indeed, our data showed that *Myc* overexpression in the MTs robustly upregulated *Fbl* and repressed *dPANK4* expression **(Fig. 5a)**. Supporting a direct regulatory role, a published chromatin immunoprecipitation followed high-throughput sequencing (ChIP-Seq) dataset of fly larvae (ENCSR191VCQ) revealed potential Myc binding sites near *dPANK4* and *Fbl* loci **(Fig. 5b)**. To confirm the direct binding of *dPANK4* and *Fbl* by Myc in our condition, we expressed HA-tagged Myc (*MT^{ts}>Myc-HA*) and performed ChIP-qPCR, which validated Myc occupancy at the promoter regions of both genes in the MTs **(Fig. 5c)**. These findings demonstrate that Myc directly regulates the expression of *dPANK4* and *Fbl* in the MTs, thereby modulating CoA biosynthesis. Given that increased MT CoA production drives ISC proliferation **(Fig. 2)**, we next tested whether *Myc* overexpression

could recapitulate this effect. Indeed, *Myc* overexpression in the MTs induced ISC proliferation in the gut **(Fig. 5d-e)**. We further found that *Myc* expression is upregulated in the MTs of mated females **(Extended Data Fig. 4b)**, consistent with the increased CoA biosynthetic activity following mating **(Fig. 2h)**. Furthermore, MT-specific knockdown of *Myc* substantially blocked mating-induced ISC proliferation **(Extended Data Fig. 4c-d)**, suggesting that mating-induced CoA biosynthesis is mediated by Myc. Altogether, these results establish Myc as a key transcriptional regulator of CoA biosynthesis in the MTs in wild-type flies.

We next examined whether Myc also mediates CoA biosynthetic pathway activation in the context of tumor growth. Notably, *Myc* expression was increased in the MTs of Yki flies **(Fig. 5f)**. Moreover, MT-specific knockdown of *Myc* in Yki flies ($Gut^{ts}>yki^{[S3A]}$, $MT^{ts}>Myc^{RNAi}$) partially restored *dPANK4* expression and suppressed *Fbl* levels **(Fig. 5g)**, suggesting that Myc drives CoA biosynthesis in the MTs of the tumor-bearing flies. Importantly, depletion of *Myc* in the MTs of Yki flies significantly reduced gut tumor cell proliferation, as evidenced by reduced gut width, decreased Yki-GFP intensity, and lower $pH3^{+}$ cell counts **(Fig. 5h-k and Extended Data Fig. 4e-l)**. Consistent with reduced tumor burden, *Myc* knockdown alleviated the bloating phenotype (**Fig. 5h, l and Extended Data Fig. 4i, m)** and significantly extended the survival of tumor-bearing flies **(Fig. 5m)**. Together, these results demonstrate that Myc expression in the MTs contributes to gut tumor growth by promoting CoA biosynthesis.

We then sought to identify the upstream signaling pathways responsible for activating *Myc* expression in the MTs. Our previous work identified several tumor-secreted cytokines, including ImpL2, Upd3, and Pvf1, that disrupt insulin, JAK-STAT, and PDGF/VEGF signaling, respectively, in various host tissues in Yki flies [29, 46, 48, 49]. Notably, *Myc* transcription is known to be inducible by multiple pathways, including PDGF signaling [50]. In line with this, we recently showed that Yki tumor-derived Pvf1 activates PDGF/VEGF receptor (Pvr) mediated JNK-Jra signaling in the MTs [51]. Consistently, overexpression of a constitutively active form of Pvr in the MTs ($MT^{ts}>Pvr^{[Act]}$) robustly increased *Myc* transcription and Myc regulon activity **(Fig. 5n and Extended Data Fig. 5n)**. Pvr activation also downregulated *dPANK4* and upregulated *Fbl* transcripts **(Fig. 5n)**, suggesting *Myc* acts downstream of Pvr signaling to regulate CoA biosynthesis. To validate this regulatory axis, we knocked down *Pvr* in the MTs of Yki flies ($Gut^{ts}>yki^{[S3A]}$, $MT^{ts}>Pvr^{RNAi}$), which reduced *Myc* expression and restored *dPANK4* and *Fbl* levels to near baseline **(Fig. 5o)**. Collectively, our findings demonstrate that Myc directly binds the promoter regions of key CoA biosynthesis genes in the MTs and orchestrates pathway activation under both physiological and tumor-associated conditions. In the tumor context, *Myc* is upregulated in the MTs in response to Pvr signaling, reprogramming host metabolism to support tumor growth **(Fig. 5p)**.

Conserved pathogenic mechanism in kidney cancer

We previously reported that PANK4 suppresses tumorigenesis in a mammalian model [9]. Our *Drosophila* studies further demonstrated that Myc enhances tumor growth by increasing CoA production specifically in the MT/kidney **(Fig. 5)**. To determine whether this MYC-CoA axis also operates in human cancer, we analyzed published ChIP-seq data from a mammalian cancer model [52] and found strong MYC occupancy at the promoters of all four PANK genes **(Extended Data Fig. 5a)**. Notably, MYC binding to *PANK1-3* promoters is prominent in the pre-tumoral and tumor samples but absent in the matched normal tissue **(Extended Data Fig. 5a)**, suggesting a tumorigenesis-related CoA biosynthesis induction by MYC. These observations are complemented by prior work that MYC enhances VB5 uptake in breast cancer to elevate CoA levels [15]. While these findings underscore a general oncogenic demand for CoA, whether the MYC-CoA axis is functionally relevant in kidney malignancy, an organ with inherently high CoA levels and strong PANK1 expression [7, 8, 53, 54], remains underexplored.

Clear Cell Renal Cell Carcinoma (ccRCC) and Papillary Renal Cell Carcinoma (pRCC) are the two major subtypes of renal cell carcinomas (RCC) [55]. Compared to ccRCC, pRCC retains tubular architecture and is thus more structurally and functionally similar to the renal tubules [55], the mammalian counterpart of *Drosophila* MTs. To assess the clinical relevance of the kidney-intrinsic MYC-CoA axis, we interrogated gene expression and survival data from both ccRCC and pRCC patients in the TCGA PanCancer Atlas cohort [56, 57]. Intriguingly, Kaplan-Meier (KM) analyses showed that high *MYC* expression was significantly associated with poorer overall survival (OS) ($p = 0.018$) and progression-free survival (PFS) ($p = 0.00052$) in pRCC patients **(Fig. 6b)**, but not in ccRCC patients **(Extended Data Fig. 5c)**, suggesting a pronounced pathogenic role for MYC in specifically in pRCC. Additionally, *MYC* expression showed a strong inverse correlation with PANK*4* expression in pRCC patients **(Extended Data Fig. 5d)**, consistent with our *Drosophila* findings that Myc suppresses *dPANK4* to promote CoA biosynthesis. We next examined the association between CoA biosynthetic gene **(Fig. 6a)** expression and clinical outcomes. In pRCC, high expression of *PANK4*, a negative regulator of CoA biosynthesis, was significantly associated with improved OS ($p = 0.016$) and PFS ($p = 0.02$) **(Fig. 6c)**. In contrast, elevated expression of genes encoding enzymes promoting CoA biosynthesis, *PANK3* and *PPAT*, predicted poorer prognosis **(Fig. 6d-e)**. Notably, these trends were not observed in ccRCC, where *PANK4* and *PPAT* expression did not correlate with survival (**Extended Data Fig. 5d-e)**, and higher *PANK3* expression was unexpectedly associated with better outcomes (**Extended Data Fig. 5f)**. These findings reveal a fundamental divergence in CoA metabolic programs between RCC subtypes and underscore a unique pathogenic role for MYC-driven activation of CoA biosynthesis specifically in pRCC.

Building on our fly findings showing that CoA biosynthesis activates the MVA-isoprenoid axis to promote cell proliferation **(Fig. 2-3)**, we next evaluated the prognostic significance of key genes in these downstream pathways **(Fig. 6a)** in pRCC. Consistent with our fly data, high expression of *FDPS* and *GGPS1*, genes encoding essential enzymes in isoprenoid backbone synthesis that generate GPP, FPP and GGPP, correlated with poorer OS ($p = 0.05$ and $p = 0.015$) and PFS ($p < 0.0001$ and $p = 0.00026$) **(Fig. 6f-g)**. These findings support a model in which enhanced isoprenoid production contributes to pRCC progression. Since FPP and GGPP are required for protein prenylation, a process known to promote proliferative signaling [20], we further examined *FNTA* (GGTase-I-alpha), an enzyme mediating this process, and found that its elevated expression was also significantly linked to reduced survival (OS: $p < 0.0001$, PFS: $p = 0.00015$) **(Extended Data Fig. 5g)**. Additionally, genes involved in the other major branches of isoprenoid metabolism, including dolichol and CoQ biosynthesis (*NUS1*, *PDSS1*, and *SRD5A3*) and cholesterol synthesis (*FDFT1* and *SQLE*), also showed significant associations with worse prognosis **(Extended Data Fig. 5h-l)**. Collectively, these results implicate multiple isoprenoid-driven processes in pRCC pathogenesis and highlight their potential prognostic and therapeutic relevance.

To further evaluate the prognostic utility of these metabolic pathways, we performed time-dependent Receiver Operating Characteristic (ROC) analyses. Multi-gene signatures for CoA biosynthesis (*PANK1-4*, *PPCS*, *PPCDC, PPAT*, and *COASY*) and isoprenoid backbone biosynthesis (*MVK*, *PMVK*, *MVD*, *IDI1*/*2*, *FDPS*, and *GGPS1*) showed strong predictive power at the 12-month mark in low-metastasis cases (AUC = 0.944 and 0.873, respectively) **(Fig. 6h-i)**, highlighting these pathways as promising early prognostic markers in pRCC. We next stratified by gender and found that the predictive performance of the CoA-biosynthesis and isoprenoid-biosynthesis signatures was more pronounced in male patients **(Extended Data Fig. 5m-p)**. Intriguingly, gene sets associated with prenylation (*FNTA*, *FNTB*, and *PGGT1B*), dolichol/CoQ biosynthesis (*DHDDS*, *NUS1, PDSS1*/*2*, and *SRD5A3*) and cholesterol synthesis (*FDFT1, SQLE, LSS, CYP51A1,* and *DHCG7*) also displayed high predictive accuracy, particularly in males **(Extended Data Fig. 5q-y)**, suggesting coordinated regulation along the CoA-isoprenoid axis and potential sex-specific clinical relevance. Collectively, our findings support a conserved role for the CoA-isoprenoid metabolic axis in pRCC progression and nominate metabolic branches within this axis as candidate targets for therapeutic intervention.

Discussion

In this study, we uncover a previously unrecognized role for Myc/MYC-driven CoA biosynthesis in orchestrating a systemic inter-organ signaling axis that governs stem cell proliferation and tumor growth. Specifically, (1) we discover that dietary VB5

supplementation is sufficient to induce ISC proliferation, revealing a novel link between vitamin intake and tissue homeostasis; (2) we identify fly MT/kidney as the primary site for CoA biosynthesis and demonstrate that renal CoA production non-autonomously promotes MVA and isoprenoid biosynthesis in the gut to stimulate ISC proliferation; (3) we show that inhibition of renal CoA biosynthesis suppresses tumor cell proliferation in a fly gut tumor model, implicating host metabolic reprogramming in supporting tumor growth; (4) we demonstrate that the oncogenic transcription factor Myc directly regulates *Fbl* and *dPANK4* in the kidney, uncovering a tissue-specific transcriptional control of CoA metabolism; (5) we establish the clinical relevance of MYC-CoA-isoprenoid axis in pRCC, highlighting its potential as both a biomarker and therapeutic target. Collectively, our findings reveal a conserved mechanism that links nutrient availability to inter-organ metabolic coordination, stem cell proliferation, and tumor progression, with broader implications for systemic metabolic regulation and therapeutic intervention in cancer.

CoA biosynthesis in inter-organ metabolic coordination

Although CoA is synthesized in nearly all tissues, its abundance varies markedly across mammalian organs, with the liver, heart, and kidney exhibiting particularly large CoA pools [7, 8]. These differences suggest that individual tissues maintain distinct CoA reservoirs to support their unique metabolic demands. Beyond their local functions, tissue-specific CoA pools may also contribute to systemic metabolic regulation in response to physiological stimuli. For instance, the hepatic CoA pool plays a central role in orchestrating the metabolic transition from the fed to the fasted state [58]. However, the physiological relevance of CoA pools in other CoA-rich organs, such as the kidney, remains poorly understood. In this study, we show that CoA is preferentially synthesized in the kidney to meet systemic CoA demands under specific physiological (e.g., mating) and pathological conditions (e.g., tumorigenesis) in *Drosophila*. Notably, the rate-determining enzyme dPANK4, a negative regulator of CoA biosynthesis, is highly enriched in this tissue, suggesting that renal CoA production is normally restrained. However, under conditions of elevated metabolic demand, such as mating or tumor growth, the CoA biosynthetic machinery in the kidney becomes activated and contributes substantially to the global CoA availability, thereby supports tissue homeostasis and stem cell/ tumor cell proliferation. CoA itself cannot cross biological membranes [7, 8], historically leading to the assumption that its function is restricted to the cell or tissue where it is synthesized. However, our findings demonstrate that CoA production in the kidney contributes to gut homeostasis in a non-autonomous manner, implying inter-organ communication via CoA-related metabolites. To reconcile this, several plausible mechanisms have been proposed in recent years. For example, 4'-phosphopantetheine, a CoA precursor downstream of VB5, can circulate systemically and may be taken up by other tissues to "jump-start" CoA biosynthesis [59, 60]. Notably, this intermediate is

thought to be the specific substrate of PANK4. Another possibility is that CoA is converted to acyl-CoAs by acyl-CoA synthetases; these acyl-CoAs can be transported between tissues and subsequently oxidized to regenerate free CoA [61]. It is therefore possible that CoA precursor intermediates or CoA derivatives are transported from the kidney to the gut. In *Drosophila*, the anatomical connection between the MTs and gut enables direct metabolite exchange. In mammals, however, whether renal CoA production contributes to systemic metabolic homeostasis via the circulation or other mechanisms remains an important avenue for future investigation. Nevertheless, our study highlights an unappreciated role for the renal CoA pool in supporting CoA demands in other organs through inter-organ metabolic exchange.

CoA-fueled isoprenoid metabolism drives proliferative signaling

While CoA metabolism is known to support fundamental processes such as TCA cycle activity and FA biosynthesis [9, 15, 62], its involvement in MVA pathway, a CoA-dependent lipid biosynthetic route, has received comparatively less attention. Our *in vivo* VB5 tracing revealed that renal activation of CoA biosynthesis increases flux to HMG-CoA, the key entry point of the MVA pathway. We further demonstrate that enhanced CoA production in the MTs boosts MVA pathway activity in the gut and promotes the biosynthesis of downstream isoprenoid metabolites, providing, to our knowledge, the first *in vivo* evidence that CoA availability directly regulates MVA/isoprenoid output. Functionally, activation of this axis drives both stem cell and tumor cell proliferation. Notably, while cholesterol is a well-known MVA-derived metabolite linked to tumor progression in mammals [22, 23], *Drosophila* lacks the cholesterol biosynthesis branch [42], allowing for focused dissection of non-sterol MVA outputs. Despite the absence of this branch, inhibition of the MVA pathway markedly suppresses cell proliferation in both VB5-supplemented and tumor-bearing flies, underscoring the functional importance of alternative downstream branches such as prenylation and CoQ/dolichol synthesis. Supporting this, inhibition of prenylation also abolished VB5 supplementation-induced ISC proliferation. Consistently, our analysis of kidney cancer pRCC reveals a pathogenic role for these isoprenoid downstream activities. While CoA biosynthesis has been implicated in supporting tumor growth by fueling the TCA cycle [15], our findings reveal an additional mechanism through which CoA metabolism contributes to tumorigenesis by promoting isoprenoid biosynthesis.

From “undruggable” MYC to targetable CoA biosynthesis

MYC is among the most frequently dysregulated oncogenes in human cancers, yet remains challenging to target directly in clinical settings [63, 64]. This limitation has fueled efforts to identify essential downstream pathways that can be therapeutically targeted in

MYC-driven tumors. In this study, we identify the CoA biosynthesis pathway as a potential metabolic vulnerability downstream of MYC activity. In *Drosophila*, the chromatin profiling and gene expression analyses indicate that Myc binds the promoter regions of both *Fbl* (homologous to mammalian *PANK1–3*) and *dPANK4*, the two key rate-limiting enzymes in CoA biosynthesis. Functionally, Myc activates *Fbl* while repressing *dPANK4*, thereby enhancing the overall CoA biosynthetic flux. This differential regulation at Myc-bound loci likely reflects the fact that MYC acts as both a transcriptional activator and repressor, depending on its interaction with cofactors such as MAX or MIZ1 [65]. Consistent with our fly data, MYC binds to promoter regions of all four *PANK* genes in mammals, and its expression inversely correlates with that of *PANK4* in human kidney cancer pRCC. These observations support a conserved role of MYC-dependent tuning of CoA production. Importantly, inhibiting CoA biosynthesis downstream of Myc suppresses tumor growth and extends survival of tumor-bearing flies. In line with these findings, we uncover a pathogenic role for MYC-driven activation of CoA biosynthesis in pRCC. Together, these findings position CoA synthesis as a tractable metabolic node in MYC-high cancers.

PDGF/VEGF signaling, classically associated with angiogenesis, is known to regulate MYC [50, 66, 67]. Our prior work demonstrates that PDGF/VEGF signaling is activated in the fly kidney by tumor-secreted Pvf1 [36]. Here, we further show that this PDGF/VEGF-MYC axis amplifies renal CoA biosynthesis, which in turn supports gut tumor growth. This tumor-host circuit highlights a previously unrecognized role for angiogenic signaling in reprogramming host organ metabolism across tissues. Therapeutically, inhibitors targeting the VEGF/PDGF axis are widely used in anti-angiogenic cancer treatment; however, resistance frequently develops, often linked to tumor metabolic adaptation under anaerobic conditions [68, 69]. Our findings suggest that targeting CoA metabolism downstream of PDGF/VEGF signaling may offer an alternative strategy to overcome these therapeutic limitations. We therefore nominate the CoA biosynthetic pathway as a metabolic vulnerability in PDGF/VEGF- and MYC-driven tumors, proposing that inhibition of CoA biosynthesis, alone or in combination with anti-angiogenic regimens, may help restrict metabolic adaptation and impede tumor progression.

CoA-isoprenoid metabolic axis as pRCC-specific vulnerability

RCC is the most common form of kidney cancer in adults, comprising two major subtypes, ccRCC ad pRCC [55]. Despite distinct molecular and clinicopathologic features between these two subtypes, current diagnostic and therapeutic approaches for pRCC are largely extrapolated from ccRCC-focused studies, resulting in only modest improvements in clinical outcomes [70-72]. Notably, pRCC is structurally and functionally closer to renal tubules, the mammalian counterpart of fly MTs, which allows our fly model to provide relevant mechanistic insight to this tumor subtype. In *Drosophila*, we define a functional

CoA-isoprenoid axis in which CoA production enhances MVA pathway activity and boosts the synthesis of downstream isoprenoid metabolites, driving stem cell proliferation and tumor growth. Extending these findings to humans, integrated transcriptomic and clinical analyses in pRCC show that high expression of CoA biosynthetic and isoprenoid pathway genes strongly correlates with poor survival, revealing potential therapeutic vulnerabilities within the CoA-isoprenoid axis. Furthermore, multi-gene signatures for CoA synthesis and terpenoid backbone synthesis display strong early predictive performance, supporting their potential as biomarkers for early-stage patient stratification. Importantly, these associations are specific to pRCC and are not observed in ccRCC. Reconciling our findings, prior cell line studies indicate that the involvement of isoprenoid metabolites in supporting proliferation varies by cell type, as supplementation with individual intermediates can sometimes rescue, but often fail to prevent, the antiproliferative effects of statins [20, 73, 74]. This heterogeneity likely reflects differences in cellular reserves of isoprenoids and the specific proliferative demands for these metabolites across cell types or tissues. Together, our cross-species analysis identifies the CoA-isoprenoid metabolic axis as a pRCC-specific vulnerability, highlighting a promising target for biomarker development and therapeutic intervention in this under-characterized cancer subtype.

Methods

Drosophila husbandry, diet, and strains

Flies were maintained on standard cornmeal-yeast-agar medium at 25 °C under a 12-hour light/dark cycle unless otherwise noted. Fly crosses were grown at 18 °C to inactivate Gal4 and LexA. Adult offspring were collected within 48 hours after eclosion, kept at 18 °C for 24-48 hours, and then shifted to 29 °C for the indicated duration to induce transgene expression (e.g., “day 3” indicates 3 days post induction). To compare virgin and mated female flies, samples were collected 72 hours after mating. For vitamin supplementation experiments, B vitamins were individually added to cooled standard fly food. The amount of vitamins was determined based on those used in *Drosophila* holidic medium protocols (see **Supplementary Table1**) [75-77]. For VB5 supplementation experiments, 2.5 mM VB5 was added to the cooled fly food unless otherwise noted. For VB5 depletion experiments, flies were fed the *Drosophila* holidic medium specifically lacking VB5 [75-77]. For simvastatin treatment experiments, 0.25 mM or 2.5 mM simvastatin were added to cooled standard fly food. Flies were fed on special diet for 72 hours before sample collection unless otherwise noted. Fly stocks used include: *esg-Gal4 (P[GawB]NP5130), tub-Gal80ts, UAS-GFP* [29], *esg-LexA::GAD* (BDSC 66632), *tub-Gal80ts, CG31272-Gal4* (MT driver) [36], *CG31272-Gal4* (BDSC 76171), *UAS-Yki3SA* [78], *LexAop-Yki3SA-GFP* [79], *UAS-CG5828-RNAi* (VDRC 27523, BDSC 57227, NIG 5828R-3), *UAS-CG5828* (this study), *UAS-Fbl-RNAi* (BDSC 64596, BDSC 35259), *UAS-Hmgcr-RNAi* (BDSC 50652),

UAS-Qm-RNAi (BDSC 65179), UAS-*β-GGT-I-RNAi* (BDSC 34687), *UAS-Mof-RNAi* (BDSC 58281), *UAS-Hat1-RNAi* (BDSC 42488), *UAS-Gcn5-RNAi* (BDSC 35601), *UAS-Smvt-RNAi* (VDRC 40650), *UAS-Myc-RNAi* (BDSC 43962, BDSC 25783), *UAS-Myc-HA* (BDSC 64759), *UAS-Drip-RNAi* (BDSC 44661, VDRC 51936), *UAS-Pvr-act* (BDSC 58496), *UAS-Pvr-RNAi* (VDRC 43459). *w1118* was used as a control. All experiments used female flies unless otherwise specified. Genotypes are listed in **Supplementary Table3**.

Immunofluorescence and Imaging

Adult guts were dissected in cold 1× PBS and fixed for 30 min in 4% formaldehyde. Tissues were washed in 0.1% 1 × PBS with 0.1% Triton X-100 (PBST) and mounted in Vectashield with DAPI (Vector Laboratories, H-1200). For pH3 staining, samples were blocked with 5% NDS in PBST, incubated with rabbit anti-pH3 (1:500, CST 9701L) overnight, followed by donkey anti-rabbit Alexa Fluor 594 (1:1,000, Invitrogen A12381) for 1 hour. After three washes in PBST, guts were mounted in Vectashield with DAPI (Vector Laboratories, H-1200). For BODIPY lipid staining, guts were dissected and fixed under the same condition mentioned above. After three times wash in 1 × PBS, the samples were incubated in BODIPY (493/503) reagent (Invitrogen D3922, 1 mg/ml in 1 × PBS) for 30 minutes. The guts were then washed three times in PBS and were mounted in Vectashield with DAPI. Confocal images were acquired on an Olympus IX83 system using FV31 software. Gut width was measured at R4-R5. $pH3^+$ cells were counted manually. GFP^+ cells were quantified by measuring the average GFP signaling strength from individual flies using Fiji-imageJ. Adult fly bloating phenotype were captured using a ZEISS Axiozoom V16 fluorescence microscope. Bloating was quantified by the abdomen-to-head area ratio using Fiji-imageJ.

Metabolite extraction, profiling, and VB5 isotope tracing in flies

Metabolites were extracted in 80% methanol. 12 adult flies or 30 dissected guts were homogenized in 1.5 ml Eppendorf tubes using 400 µl of ice-cold 80% HPLC-grade methanol and 0.5 mm zirconia beads. Following homogenization, samples were centrifuged at 20,000 × g for 5 min at 4 °C. The supernatant was transferred to a new 1.5 ml Eppendorf tube. For maximal extraction efficiency, the pellet was re-extracted with an additional 400 µl of 80% methanol using the same homogenization and centrifugation procedure, and the resulting supernatant was combined with the first. The combined extracts were vacuum dried and stored at -80 °C until analysis. Prior to analysis, dried extracts were resuspended in 20 µl of HPLC-grade water and analyzed using a hybrid 6500 QTRAP triple quadrupole mass spectrometer (AB/SCIEX) coupled to a Prominence

UFLC HPLC system (Shimadzu). Selected reaction monitoring (SRM) was used to quantify approximately 300 endogenous water-soluble metabolites. A subset of metabolites was detected in both positive and negative ion modes, yielding 311 SRM transitions through polarity switching. The HPLC gradient began at 85% buffer B (HPLC-grade acetonitrile) and ramped as follows: 85% to 42% B (0–5 min), 42% to 0% B (5–16 min), held at 0% B (16–24 min), returned to 85% B (24–25 min), and re-equilibrated at 85% B for 7 min. Buffer A consisted of 20 mM ammonium hydroxide and 20 mM ammonium acetate (pH 9.0) in 95:5 water:acetonitrile. Peak areas were integrated using MultiQuant v3.2 (AB/SCIEX), and data were analyzed using MetaboAnalyst 6.0 (https://www.metaboanalyst.ca). For VB5 isotope tracing, flies were fed on holidic medium for *Drosophila* [75-77] supplemented with 5 mM $^{13}C_3{}^{15}N_1$-labeled pantothenic acid for 48 h. 12 adult flies were collected in 1.5 ml Eppendorf tubes, and the extraction was performed following the steps above. For heavy-isotope-labelled metabolite tracing, SRMs were adapted from previous studies as detailed in our previous publication [9].

RT-qPCR of fly samples

The Nucleospin RNA kit (Macherey-Nagel) and TRIzol reagent (Thermo Fisher) was used to extract RNA from MTs and guts, respectively. cDNA was synthesized using the iScript cDNA Synthesis Kit (Bio-Rad, 1708890) and qPCR was performed with a Bio-Rad CFX96 with iQ SYBR Green Supermix (Bio-Rad). Expression was normalized to RP49 or CG13220. Primers are listed in **Supplementary Table4**.

Chromatin Immunoprecipitation (ChIP-qPCR)

ChIP was performed using the SimpleChIP Enzymatic Kit (CST 9005). Dissected MTs from adult flies with HA-tagged Myc MT-specific expression (n = 100 for each replicate) were cross-linked in 1.5% formaldehyde for 20 min at room temperature. Cross-linking was stopped by the addition of glycine solution for 5 min at room temperature. Samples were then washed twice with 1 ml 1 × PBS containing 1× Protease Inhibitor Cocktail and disaggregated using a Dounce homogenizer. Nuclei were prepared according to the manufacturer's protocol and were lysed using Diagenode Bioruptor sonicator to release the cross-linked chromatin. Chromatin was diluted in 1 × ChIP buffer and incubated with 10 µl HA-tagged rabbit monoclonal antibodies (CST 3724) or normal rabbit IgG (CST 2729) overnight at 4 °C with rotation. 30 µl of ChIP-Grade Protein G Magnetic Beads (CST 9006) was incubated with each immunoprecipitation for 2 hours at 4 °C with rotation. Beads were washed and incubated in 150 µl 1 × ChIP Elution Buffer at 65 °C for 30 min with vertexing to elute the chromatin. Cross-links were reversed by adding 6 µl 5 M NaCl and 2 µl Proteinase K to the eluted chromatin supernatant and incubating 2 h at 65 °C,

followed by DNA purification step. 1 μl DNA sample was used as template for qPCR to detect enrichments of certain DNA regions. qPCR of a fragment in the *Tll* gene region was used as the negative control. Primer sequences are detailed in the Supplementary Data.

Survival curve of flies

Survival of flies was analyzed by calculating the percentage of flies alive in each vial incubated at 29 °C. Flies were placed in vials with fresh food, and the number of alive flies were counted daily.

Public datasets and statistical analyses

Transcriptome and survival data were retrieved from TCGA PanCancer Atlas (KIRP and KIRC) via cBioPortal [56, 57]. Kaplan-Meier (KM) survival curves were generated using the R packages survival and survminer. Time-dependent ROC analysis used the timeROC package, stratified by time point, metastasis status, and gender. hdWGCNA (0.4.05) was used to predict regulon activity using snRNA-sequencing datasets. Briefly, each dataset was subset to the clusters labelled as Malpighian tubule and ran through the hdWGCNA transcription factory regulatory network analysis pipeline using default settings (https://smorabit.github.io/hdWGCNA/articles/tf_network.html). The FindDifferentialRegulons() function was used to perform differential expression analysis on regulon scores/activity. GraphPad Prism was used for all statistical analyses. *p*-values were calculated via unpaired two-tailed *t*-test or one-way ANOVA unless stated. Gene expression was normalized to controls. *n* represents biological replicates. Error bars indicate s.d. Biorender was used for illustrations. ChatGPT assisted in proofreading; all content was verified and revised by the authors.

Acknowledgements

We thank R. Binari, J. Zirin, L. Liu, C. Villalta, S. Mohr, K. Huang, A. Carte, B. Xia, A.R.Kim and all members of the Perrimon lab for their critical suggestions and help on this research. We thank P. M. Llopis, P. V. Anekal, A. Wells, and Microscopy Resources on the North Quad (MicRoN) core facility at Harvard Medical School for advice and help with confocal imaging. We thank the *Drosophila* RNAi Screening Center (DRSC), Bloomington Drosophila Stock Center (BDSC), Vienna *Drosophila* Resource Center (VDRC), and Fly Stocks of National Institute of Genetics (NIG) for providing fly stocks used in this study. We thank FlyBase for the genetics knowledgebase and database resource. This work is funded in part by NIH/NIDDK

(R56DK140239 and R01DK140239) (C.C.D) and by the CANCAN team supported by the Cancer Grand Challenges partnership funded by Cancer Research UK (CGCATF-2021/100022) and the National Cancer Institute (1 OT2 CA278685-01). T. M. is supported by the Cystinosis Research Foundation and the Glenn Foundation for Medical Research Postdoctoral Fellowship in Aging Research. Y.L. is supported by the Charles A. King Trust Fellowship. N.P. is an investigator at the Howard Hughes Medical Institute. This article is subject to HHMI's Open Access to Publications policy. HHMI lab heads have previously granted a non-exclusive CC BY 4.0 license to the public and a sublicensable license to HHMI in their research articles. Pursuant to those licenses, the author-accepted manuscript of this article can be made freely available under a CC BY 4.0 license immediately upon publication.

Author contributions

T.M., C.D., and N.P. conceived the study and designed the experiments. T.M. conducted the majority of the experiments and the data analysis. T.M., C.D., J.A., and Y.L. designed and conducted the metabolomics studies. T.M., and X.S conducted the molecular cloning experiments for transgenic fly lines. Y.L., M.Q., and Y.H. were responsible for the bioinformatics analysis. T.M., Y.H., C.D., and N.P. interpreted the results. T.M. and N.P. wrote the manuscript with contributions and feedback from all authors. All authors reviewed and approved the final manuscript.

Figure 1

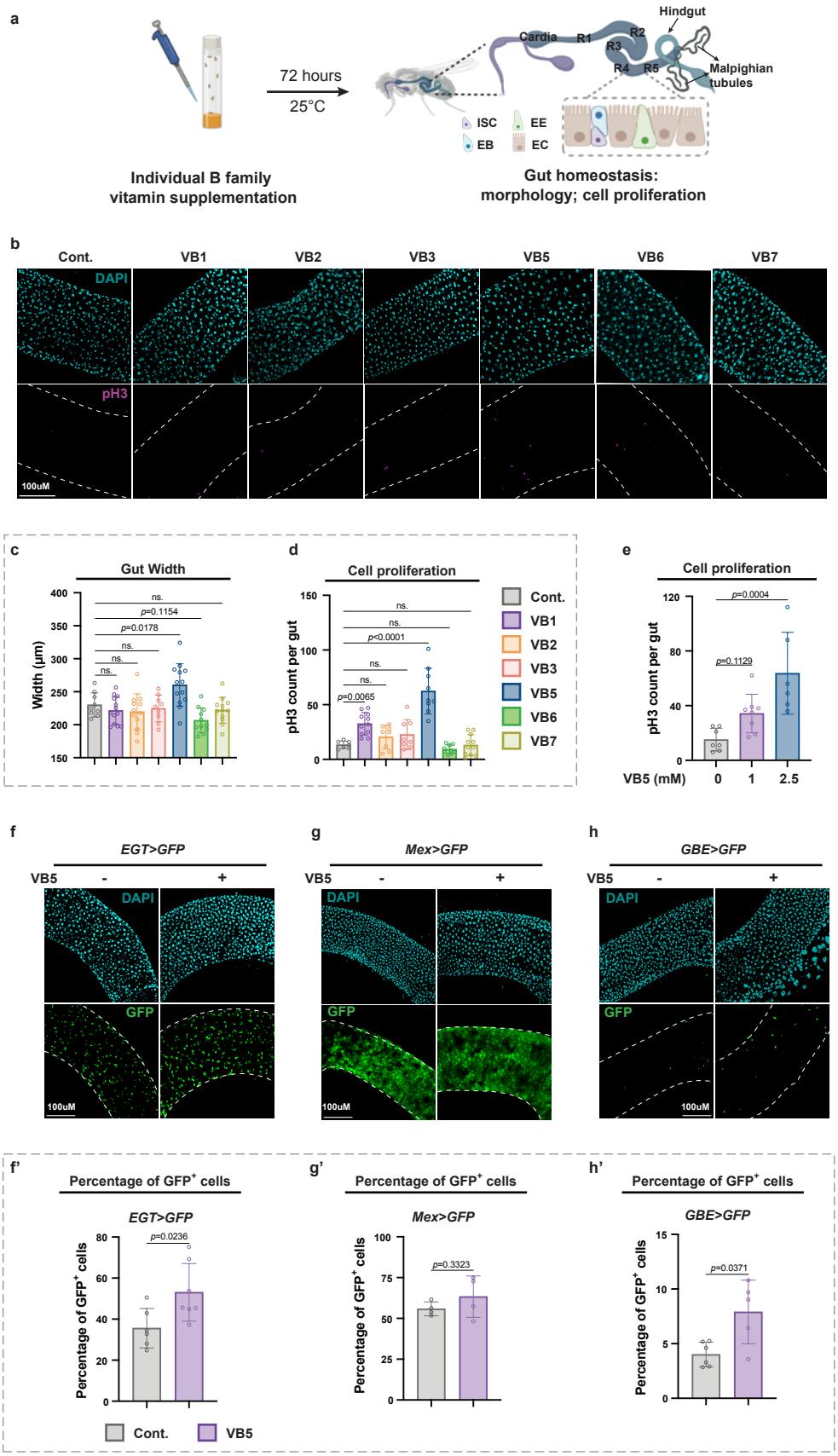
a
72 hours
25°C
Individual B family vitamin supplementation
Cardia
R1
R2
R3
R4
R5
Hindgut
Malpighian tubules
ISC
EB
EE
EC
Gut homeostasis: morphology; cell proliferation
b
Cont.
VB1
VB2
VB3
VB5
VB6
VB7
DAPI
pH3
100uM
c
Gut Width
Width (µm)
ns.
p=0.1154
p=0.0178
d
Cell proliferation
pH3 count per gut
p<0.0001
p=0.0065
e
Cell proliferation
p=0.0004
p=0.1129
VB5 (mM)
0
1
2.5
f
EGT>GFP
g
Mex>GFP
h
GBE>GFP
VB5
GFP
f'
g'
h'
Percentage of GFP+ cells
p=0.0236
p=0.3323
p=0.0371

Fig. 1 | VB5 supplementation stimulates intestinal stem cell ISC proliferation. a, Experimental design for individual B vitamin supplementation and assessment of gut homeostasis. The *Drosophila* midgut is composed of five regions (R1-R5) with distinct cell types. The Malpighian tubules (MTs) are connected to the posterior midgut. ISC, intestinal stem cell; EB, enteroblast; EC, enterocyte; EE, enteroendocrine cell. **b,** Representative images of midguts from flies supplemented with VB1, VB2, VB3, VB5, VB6, VB7, and control (Cont.). Vitamin concentrations were determined based on those used in *Drosophila* holidic medium protocols (see **Methods** and **Supplementary Table1**). **c,** Quantification of midgut width after individual B vitamin supplementation. Each dot represents one midgut. n = 10-14. **d,** Quantification of phospho-Histone 3-positive ($pH3^+$) cells per midgut after individual B vitamin supplementation. n = 8-12. Both VB1 and VB5 increased $pH3^+$ cell counts, with VB5 inducing the most robust response and thus selected for further investigation. **e,** Quantification of $pH3^+$ cells per midgut following VB5 supplementation at 0, 1, or 2.5 mM. n = 7. **f, h, j,** Representative images of guts showing GFP expression in ISC/EB (*EGT*>) (**f**), EB (*GBE*>) (**h**), and EC (*Mex*>) (**j**) cell populations. **f', h', j',** Quantification of GFP intensity from panel **f, h,** and **j**, respectively. n = 4-6. Statistical significance assessed by ordinary one-way ANOVA (**c, e**) and unpaired two-sided Student's *t*-test (**f', h', j'**). Error bars indicate s.d., with means at the center. **a** created with BioRender.

Figure 2

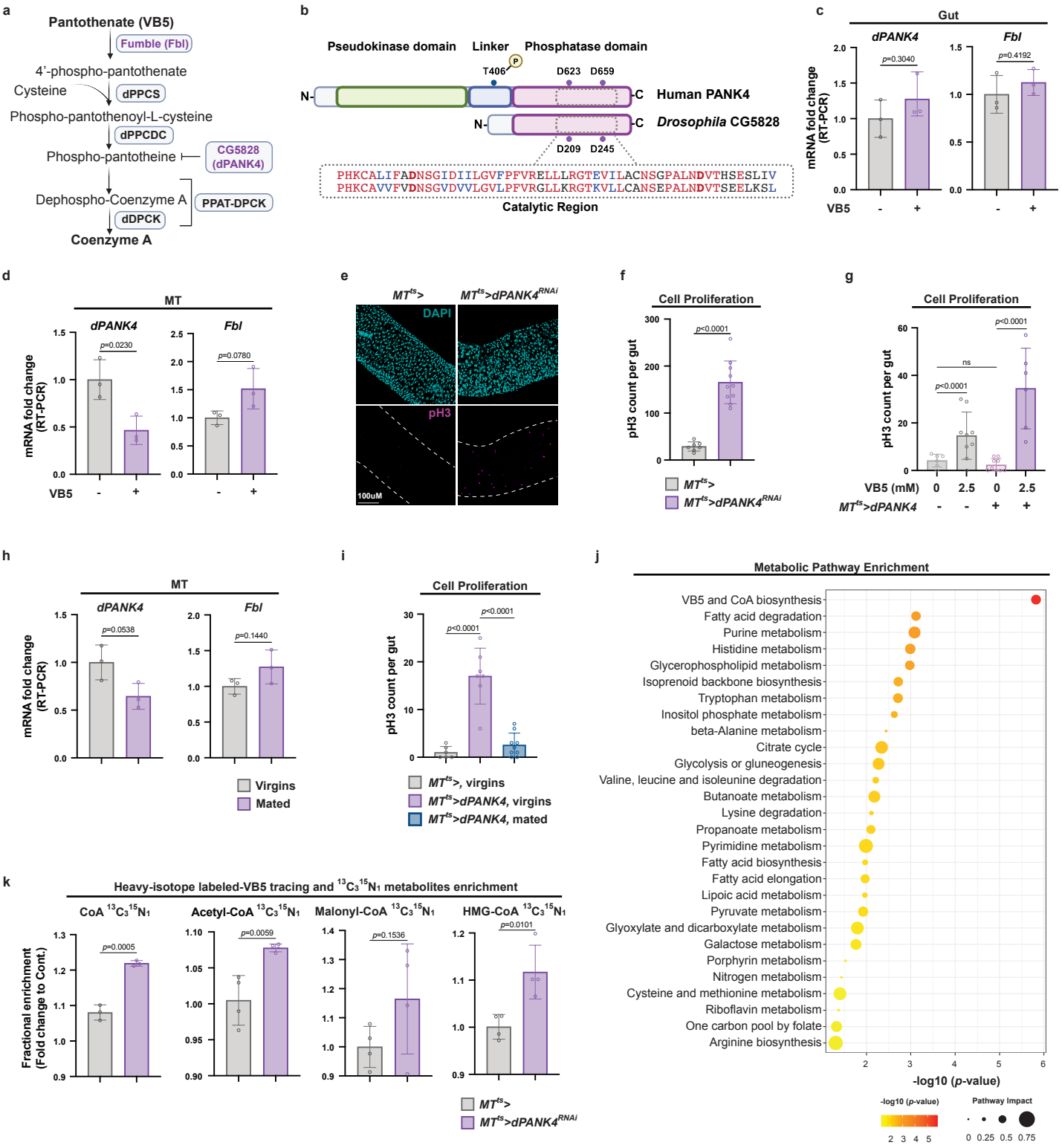
a
Pantothenate (VB5)
Fumble (Fbl)
4'-phospho-pantothenate
Cysteine
dPPCS
Phospho-pantothenoyl-L-cysteine
dPPCDC
Phospho-pantotheine
CG5828 (dPANK4)
Dephospho-Coenzyme A
PPAT-DPCK
dDPCK
Coenzyme A
b
Pseudokinase domain
Linker
Phosphatase domain
T406
D623
D659
N-
-C
Human PANK4
Drosophila CG5828
D209
D245
PHKCALIFADNSGIDIILGVFPFVRELLLRGTEVILACNSGPALNDVTHSESLIV
PHKCAVVFVDNSGVDVVLGVLPFVRGLLKRGTKVLLCANSEPALNDVTSEELKSL
Catalytic Region
c
Gut
dPANK4
Fbl
p=0.3040
p=0.4192
mRNA fold change (RT-PCR)
VB5
d
MT
dPANK4
Fbl
p=0.0230
p=0.0780
mRNA fold change (RT-PCR)
VB5
e
MTts>
MTts>dPANK4RNAi
DAPI
pH3
100uM
f
Cell Proliferation
p<0.0001
pH3 count per gut
MTts>
MTts>dPANK4RNAi
g
Cell Proliferation
p<0.0001
ns
p<0.0001
pH3 count per gut
VB5 (mM)
MTts>dPANK4
h
MT
dPANK4
Fbl
p=0.0538
p=0.1440
mRNA fold change (RT-PCR)
Virgins
Mated
i
Cell Proliferation
p<0.0001
p<0.0001
pH3 count per gut
MTts>, virgins
MTts>dPANK4, virgins
MTts>dPANK4, mated
j
Metabolic Pathway Enrichment
VB5 and CoA biosynthesis
Fatty acid degradation
Purine metabolism
Histidine metabolism
Glycerophospholipid metabolism
Isoprenoid backbone biosynthesis
Tryptophan metabolism
Inositol phosphate metabolism
beta-Alanine metabolism
Citrate cycle
Glycolysis or gluneogenesis
Valine, leucine and isoleunine degradation
Butanoate metabolism
Lysine degradation
Propanoate metabolism
Pyrimidine metabolism
Fatty acid biosynthesis
Fatty acid elongation
Lipoic acid metabolism
Pyruvate metabolism
Glyoxylate and dicarboxylate metabolism
Galactose metabolism
Porphyrin metabolism
Nitrogen metabolism
Cysteine and methionine metabolism
Riboflavin metabolism
One carbon pool by folate
Arginine biosynthesis
-log10 (p-value)
Pathway Impact
k
Heavy-isotope labeled-VB5 tracing and 13C3 15N1 metabolites enrichment
CoA 13C3 15N1
Acetyl-CoA 13C3 15N1
Malonyl-CoA 13C3 15N1
HMG-CoA 13C3 15N1
p=0.0005
p=0.0059
p=0.1536
p=0.0101
Fractional enrichment (Fold change to Cont.)
MTts>
MTts>dPANK4RNAi

Fig. 2 | CoA biosynthesis in the Malpighian tubules (MTs) non-autonomously regulates ISC proliferation. a, Schematic of the CoA biosynthesis pathway in *Drosophila*. Fbl (fumble), ortholog of mammalian PANK1–3; PPCS, Phosphopantothenoylcysteine Synthetase; PPCDC, Phosphopantothenoylcysteine Decarboxylase; PPAT, Phosphopantetheine Adenylyltransferase; DPCK, Dephospho-CoA Kinase. PPAT and DPCK activities are combined in a single bifunctional enzyme in many eukaryotes, known as PPAT-DPCK or COASY (Coenzyme A Synthase). **b,** Amino acid sequence alignment of the catalytic region between human PANK4 and *Drosophila* CG5828 (dPANK4). See also **Extended Data Fig. 1** for full-length alignment. **c, d,** qRT-PCR analysis of *dPANK4* and *Fbl* mRNA levels in guts (**c**) and MTs (**d**) of flies with or without dietary VB5 supplementation. Each dot represents a biological replicate. n = 3. **e,** Representative images of guts in flies with or without MT-specific *dPANK4* knockdown at day 10. **f,** Quantification of $pH3^+$ cells per midgut from **e**. n = 8-10. **g,** $pH3^+$ cell counts per midgut in flies with or without MT-specific *dPANK4* knockdown, fed diets with or without VB5 depletion. **h,** qRT-PCR analysis of *dPANK4* and *Fbl* mRNA levels in MTs from virgin or mated female flies. n = 3. **i,** Quantification $pH3^+$ cells per midgut in virgin or mated female flies with or without MT *dPANK4* overexpression at day 7. n = 6-9. See also **Extended Data Fig. 1** for representative gut images for panel **i** and validation of this phenotype with independent fly lines. **j,** Pathway enrichment analysis of whole-fly metabolomics profiling of flies with MT-specific *dPANK4* knockdown versus controls at day 9. The top enriched KEGG pathways are shown, ranked by statistical significance (-log10(*p*-value)) and colored accordingly. Dot size represents pathway value. n = 5. **k,** Relative levels of $[^{13}C^{15}N]$-labeled CoA, acetyl-CoA, malonyl-CoA, and HMG-CoA in MT-specific *dPANK4* knockdown versus controls at day 9. n = 4. Statistical significance assessed by unpaired two-sided Student's *t*-test (**c-d, f, h, k**), one-way ANOVA (**g, i**), and Fisher's exact test (**j**). Error bars indicate s.d., with means at the center. **b** created with BioRender.

Figure 3

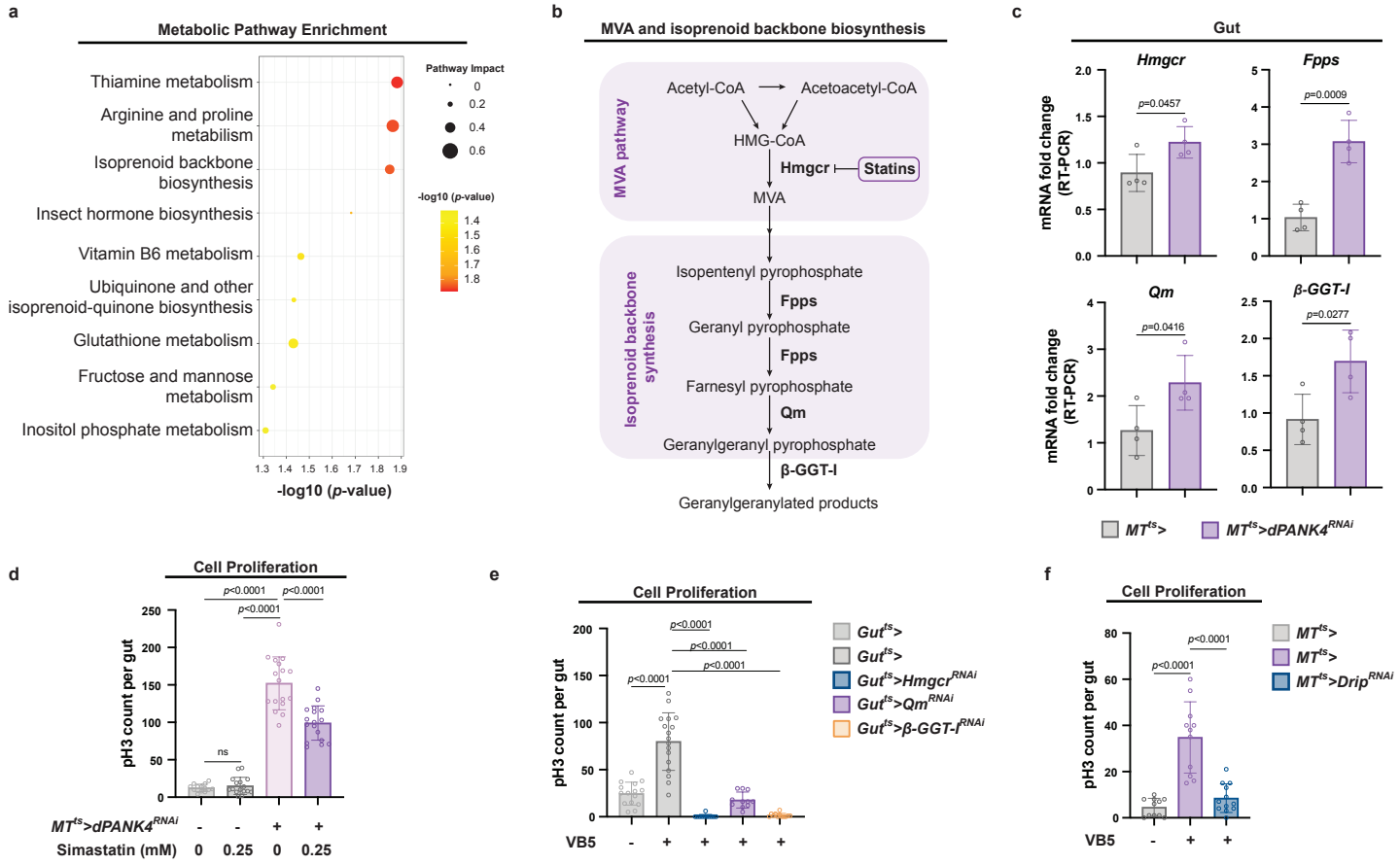
a
Metabolic Pathway Enrichment
Thiamine metabolism
Arginine and proline metabolism
Isoprenoid backbone biosynthesis
Insect hormone biosynthesis
Vitamin B6 metabolism
Ubiquinone and other isoprenoid-quinone biosynthesis
Glutathione metabolism
Fructose and mannose metabolism
Inositol phosphate metabolism
-log10 (p-value)
Pathway Impact
0
0.2
0.4
0.6
-log10 (p-value)
1.4
1.5
1.6
1.7
1.8
b
MVA and isoprenoid backbone biosynthesis
MVA pathway
Acetyl-CoA
Acetoacetyl-CoA
HMG-CoA
Hmgcr
Statins
MVA
Isoprenoid backbone synthesis
Isopentenyl pyrophosphate
Fpps
Geranyl pyrophosphate
Fpps
Farnesyl pyrophosphate
Qm
Geranylgeranyl pyrophosphate
β-GGT-I
Geranylgeranylated products
c
Gut
Hmgcr
Fpps
Qm
β-GGT-I
mRNA fold change (RT-PCR)
p=0.0457
p=0.0009
p=0.0416
p=0.0277
MTts>
MTts>dPANK4RNAi
d
Cell Proliferation
pH3 count per gut
p<0.0001
ns
MTts>dPANK4RNAi
Simastatin (mM)
0
0.25
e
Cell Proliferation
pH3 count per gut
Gutts>
Gutts>Hmgcr RNAi
Gutts>Qm RNAi
Gutts>β-GGT-I RNAi
VB5
f
Cell Proliferation
pH3 count per gut
MTts>
MTts>Drip RNAi
VB5

Fig. 3 | MT CoA production promotes gut mevalonate (MVA) and isoprenoid backbone biosynthesis. a, Pathway enrichment analysis of gut metabolomics profiling of flies with MT-specific *dPANK4* knockdown versus controls at day 9. The top enriched KEGG pathways are shown, ranked by statistical significance (-log10(*p*-value)) and colored accordingly. Dot size represents pathway value. n = 4. **b,** Schematic of mevalonate (MVA) and isoprenoid biosynthesis pathway in *Drosophila*. Hmgcr, HMG-CoA reductase; Fpps, Farnesyl pyrophosphate synthase; Qm, Quasimodo, *Drosophila* homolog of geranylgeranyl diphosphate synthase; β-GGT-I, β subunit of Geranylgeranyltransferase type I (GGTase-I). **c,** qRT-PCR analysis of *Hmgcr*, *Fpps*, *Qm*, and *β GGT-I* mRNA levels in guts from MT-specific *dPANK4* knockdown and control flies at day 9. n = 4. **d,** Quantification of $pH3^+$ cells per midgut in flies with or without MT *dPANK4* depletion, fed on normal or simvastatin-containing diet. See also **Extended Data Fig. 2** for effect under another dose of simvastatin treatment. **e,** $pH3^+$ cell quantification in control flies or flies with gut-specific knockdown of *Hmgcr*, *Qm*, or *β-GGT-I* under VB5 supplementation. n = 10-15. **f,** $pH3^+$ cell quantification per midgut in control flies and flies with MT *Drip* knockdown under VB5 supplementation. n = 10-15. Statistical significance assessed by unpaired two-sided Student's *t*-test (**c**), one-way ANOVA (**d-f**), and Fisher's exact test (**a**). Error bars indicate s.d., with means at the center.

Figure 4

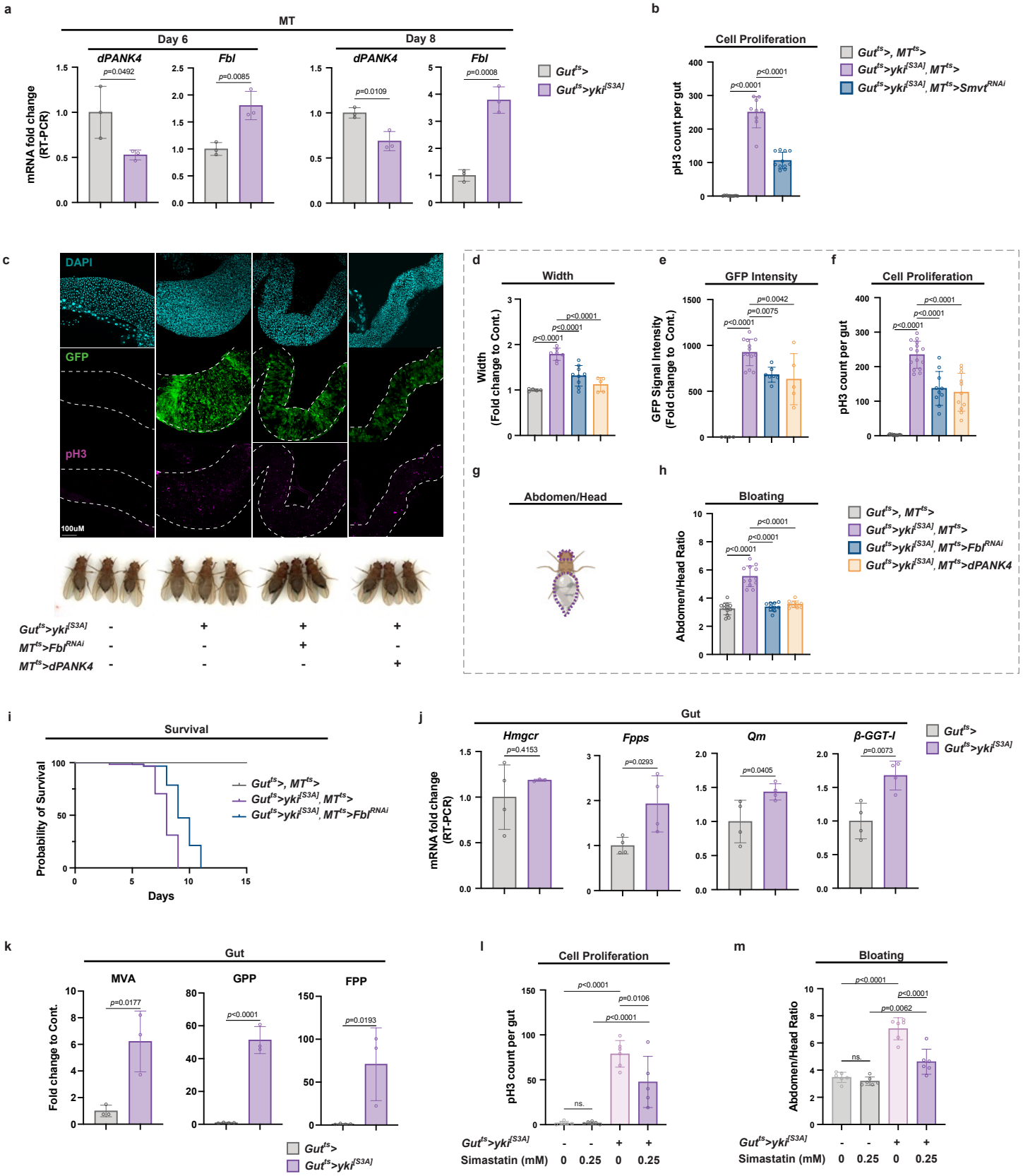
a
MT
Day 6
Day 8
dPANK4
Fbl
mRNA fold change (RT-PCR)
p=0.0492
p=0.0085
p=0.0109
p=0.0008
Gut^ts>
Gut^ts>yki^[S3A]
b
Cell Proliferation
pH3 count per gut
p<0.0001
Gut^ts>, MT^ts>
Gut^ts>yki^[S3A], MT^ts>
Gut^ts>yki^[S3A], MT^ts>Smvt^RNAi
c
DAPI
GFP
pH3
100uM
Gut^ts>yki^[S3A]
MT^ts>Fbl^RNAi
MT^ts>dPANK4
d
Width
Width (Fold change to Cont.)
e
GFP Intensity
GFP Signal Intensity (Fold change to Cont.)
p=0.0042
p=0.0075
f
Cell Proliferation
pH3 count per gut
g
Abdomen/Head
h
Bloating
Abdomen/Head Ratio
Gut^ts>, MT^ts>
Gut^ts>yki^[S3A], MT^ts>
Gut^ts>yki^[S3A], MT^ts>Fbl^RNAi
Gut^ts>yki^[S3A], MT^ts>dPANK4
i
Survival
Probability of Survival
Days
Gut^ts>, MT^ts>
Gut^ts>yki^[S3A], MT^ts>
Gut^ts>yki^[S3A], MT^ts>Fbl^RNAi
j
Gut
Hmgcr
Fpps
Qm
β-GGT-I
mRNA fold change (RT-PCR)
p=0.4153
p=0.0293
p=0.0405
p=0.0073
Gut^ts>
Gut^ts>yki^[S3A]
k
Gut
MVA
GPP
FPP
Fold change to Cont.
p=0.0177
p<0.0001
p=0.0193
Gut^ts>
Gut^ts>yki^[S3A]
l
Cell Proliferation
pH3 count per gut
p<0.0001
p=0.0106
ns.
Gut^ts>yki^[S3A]
Simastatin (mM)
0
0.25
m
Bloating
Abdomen/Head Ratio
p<0.0001
p=0.0062
ns.
Gut^ts>yki^[S3A]
Simastatin (mM)
0
0.25

Fig. 4 | MT CoA biosynthesis promotes gut tumor growth. a, qRT-PCR analysis of *dPANK4* and *Fbl* mRNA levels in MTs from Yki and control flies at day 6 and 8. n = 3. **b,** $pH3^+$ cell quantification in control flies and Yki flies with or without MT-specific *Smvt* knockdown at day 5. **c,** Representative images of guts (day 5) and representative images of phenotypes (day 6) from control flies and Yki flies with or without MT-specific *Fbl* knockdown or *dPANK4* overexpression. **D-f,** Quantification of gut width (**d**), GFP intensity (**e**), and $pH3^+$ cell counts (**f**). n = 6-8. See also **Extended Data Fig. 3** for phenotypes at day 3 and validations using independent fly lines. **g-h,** Quantification method (**g**) and results (**h**) for bloating phenotypes shown in (**c**), defined as abdomen-to-head area ratio. n = 6-8. See **Extended Data Fig. 3** for validation with independent lines. **i,** Survival curves of control, Yki, and Yki flies with MT *Fbl* depletion. n = 40-45. **j,** qRT-PCR analysis of *Hmgcr*, *Fpps*, *Qm*, and *β GGT-I* mRNA levels in guts from Yki or control flies at day 6. n = 4. **k,** Relative metabolite levels of mevalonate (MVA), geranyl pyrophosphate (GPP), and farnesyl pyrophosphate (FPP) retrieved from metabolomics analysis (n = 4). **l,** $pH3^+$ cell quantification in control flies and Yki flies with or without simvastatin treatment at day 5. **m,** Quantification of bloating in control flies and Yki flies with or without simvastatin treatment at day 6. n = 12. Also see **Extended Data Fig. 3** for representative images of bloating phenotypes. Statistical significance assessed by unpaired two-sided Student's *t*-test (**a, j-k**), one-way ANOVA (**b, d-f, h, l-m)**, and log-rank (Mantel–Cox) test (**i**). Error bars indicate s.d., with means at the center.

Figure 5

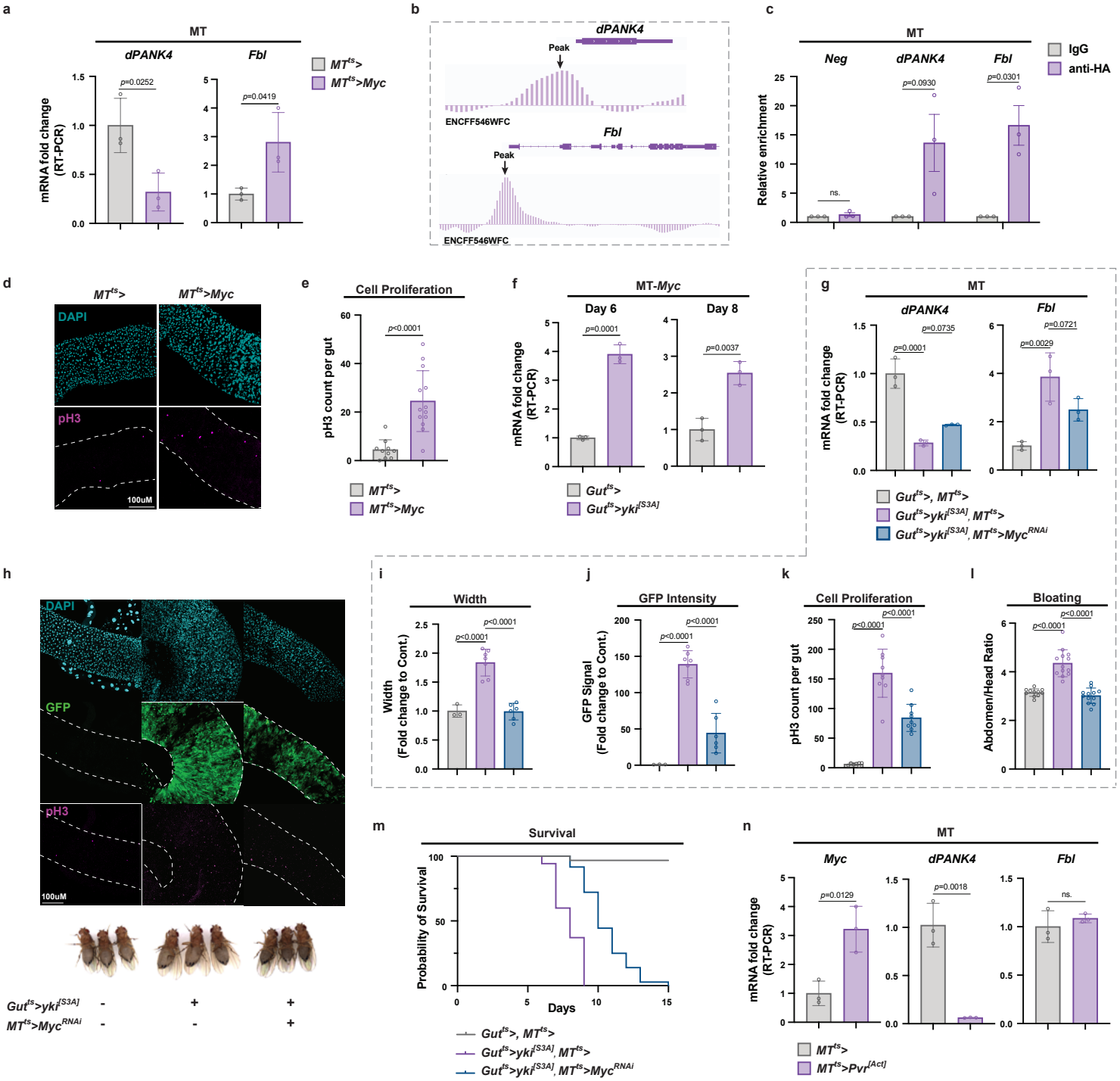
a
MT
dPANK4
Fbl
mRNA fold change (RT-PCR)
p=0.0252
p=0.0419
MTts>
MTts>Myc
b
dPANK4
Peak
ENCFF546WFC
Fbl
Peak
ENCFF546WFC
c
MT
Neg
dPANK4
Fbl
Relative enrichment
ns.
p=0.0930
p=0.0301
IgG
anti-HA
d
MTts>
MTts>Myc
DAPI
pH3
100uM
e
Cell Proliferation
pH3 count per gut
p<0.0001
MTts>
MTts>Myc
f
MT-Myc
Day 6
Day 8
mRNA fold change (RT-PCR)
p=0.0001
p=0.0037
Gutts>
Gutts>yki[S3A]
g
MT
dPANK4
Fbl
mRNA fold change (RT-PCR)
p=0.0001
p=0.0735
p=0.0721
p=0.0029
Gutts>, MTts>
Gutts>yki[S3A], MTts>
Gutts>yki[S3A], MTts>MycRNAi
h
DAPI
GFP
pH3
100uM
Gutts>yki[S3A] - + +
MTts>MycRNAi - - +
i
Width
Width (Fold change to Cont.)
p<0.0001
p<0.0001
j
GFP Intensity
GFP Signal (Fold change to Cont.)
p<0.0001
p<0.0001
k
Cell Proliferation
pH3 count per gut
p<0.0001
p<0.0001
l
Bloating
Abdomen/Head Ratio
p<0.0001
p<0.0001
m
Survival
Probability of Survival
Days
Gutts>, MTts>
Gutts>yki[S3A], MTts>
Gutts>yki[S3A], MTts>MycRNAi
n
MT
Myc
dPANK4
Fbl
mRNA fold change (RT-PCR)
p=0.0129
p=0.0018
ns.
MTts>
MTts>Pvr[Act]
o
MT
Myc
dPANK4
Fbl
mRNA fold change (RT-PCR)
p=0.0037
p=0.0170
p=0.0043
p=0.0408
p=0.0358
p=0.0707
Gutts>, MTts>
Gutts>yki[S3A], MTts>
Gutts>yki[S3A], MTts>PvrRNAi
p
Kidney
Gut
Myc
Fbl
dPANK4
Tumor-derived Pvf1
VB5
CoA
Metabolites
Water influx
Mevalonate and isoprenoid biosynthesis
De novo CoA biosynthesis
Gut homeostasis and tumor progression

Fig. 5 | *Myc* transcriptionally regulates CoA biosynthesis genes in the MTs. a, qRT-PCR analysis of *dPANK4* and *Fbl* mRNA levels in MTs from *Myc*-overexpressing versus control flies at day 7. **b,** Data from the ChIP-seq database indicating enrichment of Myc binding at the *dPANK4* and *Fbl* loci. **c,** ChIP-qPCR showing enrichment of HA-tagged Myc binding at the *dPANK4* and *Fbl* gene regions, shown by fold changes relative to control IgG (n = 3). Neg, negative control. **d-e,** Representative gut images (**d**) and $pH3^+$ cell quantification (**e**) in *Myc*-overexpressing versus control flies. n = 10-12. **f,** qRT-PCR analysis of *Myc* mRNA level in MTs from Yki or control flies at day 6 and 8. **g,** qRT-PCR analysis of *dPANK4* and *Fbl* mRNA levels in MTs from control and Yki flies with or without MT *Myc* depletion. **h,** Representative gut tumor images (day 5) and representative images of phenotypes (day 6) from control and Yki flies with or without MT-specific *Myc* knockdown. **i–k,** Quantification of gut width (**i**), GFP intensity (**j**), and $pH3^+$ cell counts (**k**). n = 6-8. See also **Extended Data Fig. 4** for phenotypes at day 3 and validations using independent fly lines. **l,** Bloating quantification via abdomen-to-head ratio. n = 12. See **Extended Data Fig. 4** for validation with independent lines. **m,** Survival curve of control and Yki flies with or without MT *Myc* knockdown. n = 40-45. **n,** qRT-PCR analysis of *Myc*, *dPANK4*, and *Fbl* mRNA levels in MTs from control and MT *Pvr* activation flies. n=3. **o,** qRT-PCR analysis of *Myc*, *dPANK4*, and *Fbl* mRNA levels in MTs of control and Yki flies with or without MT *Pvr* depletion. **p,** Summary model of the gut-kidney axis in *Drosophila*. Statistical significance assessed by unpaired two-sided Student's *t*-test (**a, c, e, f, n**), one-way ANOVA (**g, i-l, o)**, and log-rank (Mantel–Cox) test (**m**). Error bars indicate s.d., with means at the center.

Figure 6

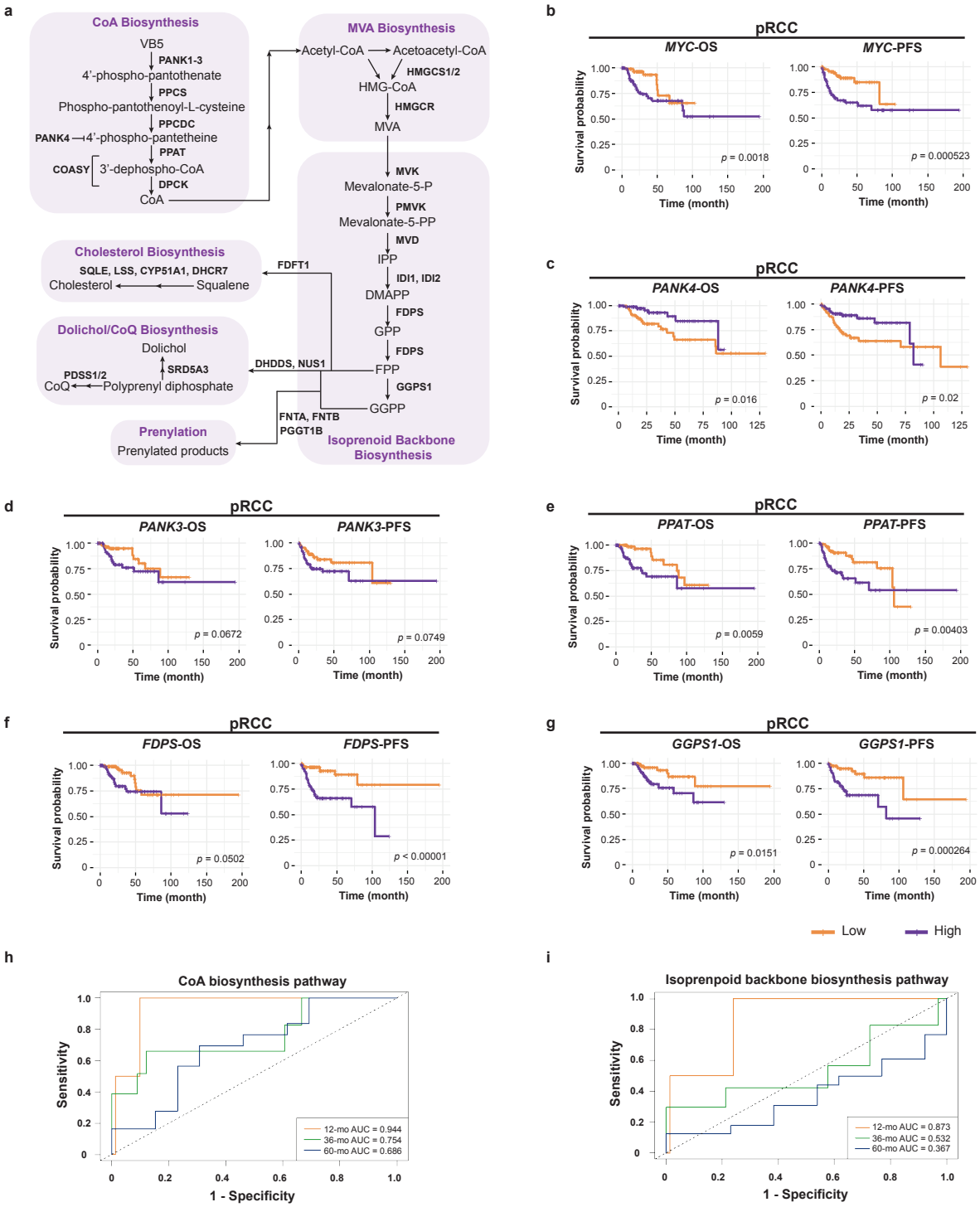
a
CoA Biosynthesis
VB5
PANK1-3
4'-phospho-pantothenate
PPCS
Phospho-pantothenoyl-L-cysteine
PPCDC
PANK4
4'-phospho-pantetheine
PPAT
COASY
3'-dephospho-CoA
DPCK
CoA
MVA Biosynthesis
Acetyl-CoA
Acetoacetyl-CoA
HMGCS1/2
HMG-CoA
HMGCR
MVA
MVK
Mevalonate-5-P
PMVK
Mevalonate-5-PP
MVD
IPP
IDI1, IDI2
DMAPP
FDPS
GPP
FDPS
FPP
GGPS1
GGPP
Isoprenoid Backbone Biosynthesis
Cholesterol Biosynthesis
SQLE, LSS, CYP51A1, DHCR7
Cholesterol
Squalene
FDFT1
Dolichol/CoQ Biosynthesis
Dolichol
SRD5A3
PDSS1/2
CoQ
Polyprenyl diphosphate
DHDDS, NUS1
FNTA, FNTB
PGGT1B
Prenylation
Prenylated products
b
pRCC
MYC-OS
MYC-PFS
p = 0.0018
p = 0.000523
c
pRCC
PANK4-OS
PANK4-PFS
p = 0.016
p = 0.02
d
pRCC
PANK3-OS
PANK3-PFS
p = 0.0672
p = 0.0749
e
pRCC
PPAT-OS
PPAT-PFS
p = 0.0059
p = 0.00403
f
pRCC
FDPS-OS
FDPS-PFS
p = 0.0502
p < 0.00001
g
pRCC
GGPS1-OS
GGPS1-PFS
p = 0.0151
p = 0.000264
Survival probability
Time (month)
Low
High
h
CoA biosynthesis pathway
12-mo AUC = 0.944
36-mo AUC = 0.754
60-mo AUC = 0.686
i
Isoprenpoid backbone biosynthesis pathway
12-mo AUC = 0.873
36-mo AUC = 0.532
60-mo AUC = 0.367
Sensitivity
1 - Specificity

Fig. 6 | Conserved pathogenic mechanism in kidney cancer. a, Schematic of CoA, MVA, and isoprenoid backbone pathways and their downstream branches in humans, including cholesterol biosynthesis, dolichol and ubiquinone (CoQ) biosynthesis, and protein prenylation. HMGCS1/2, HMG-CoA synthase 1/2; HMGCR, HMG-CoA reductase; MVK, mevalonate kinase; PMVK, phosphomevalonate kinase; MVD, mevalonate diphosphate decarboxylase; IDI1/2, isopentenyl-diphosphate delta isomerase 1/2; FDPS, farnesyl diphosphate synthase; GGPS1, geranylgeranyl diphosphate synthase 1; FDFT1, farnesyl-diphosphate farnesyltransferase 1 (also known as squalene synthase); SQLE, squalene epoxidase; LSS, lanosterol synthase; CYP51A1, cytochrome P450 family 51 subfamily A member 1; DHCR7, 7-dehydrocholesterol reductase; DHDDS, dehydrodolichyl diphosphate synthase subunit; NUS1, Nogo-B receptor; PDSS1/2, decaprenyl-diphosphate synthase subunit 1/2; SRD5A3, steroid 5 alpha-reductase 3; FNTA, farnesyltransferase, alpha subunit; FNTB, farnesyltransferase, beta subunit; PGGT1B, protein geranylgeranyltransferase type I, beta subunit. IPP, isopentenyl pyrophosphate; DMAPP, dimethylally pyrophosphate; GPP, geranyl pyrophosphate; FPP, farnesyl pyrophosphate; GGPP, geranylgeranyl pyrophosphate. **b–g,** Kaplan-Meier (KM) survival analyses of overall survival (OS) and progression-free survival (PFS) for 188 Papillary Renal Cell Carcinoma (pRCC/KIRP) patients with low (bottom third) versus high (top third) expression of *MYC* (**b**), *PANK4* (**c**), *PANK3* (**d**), *PPAT* (**e**), *FDPS* (**f**), and *GGPS1* (**g**); the graph is based on data from the PanCancer Atlas of the TCGA. **h-i,** Time-dependent receiver operating characteristic (ROC) curve analysis showing the prognostic performance (area under the curve, AUC) of gene expression signatures from the CoA biosynthesis pathway (**h**) (n = 91) and the isoprenoid backbone synthesis pathway (**i**) (n = 91) in pRCC patients. AUC values were calculated at 12, 24, and 36 months of metastasis stage M0. Pathway gene sets include: CoA biosynthesis: *PANK1-4, PPCS, PPCDC, PPAT* and *COASY*; isoprenoid backbone synthesis: *MVK, PMVK, MVD, IDI1, IDI2, FDPS* and *GGPS1*. Statistical significance assessed by log-rank (Mantel–Cox) test (**b–g**) and AUC analysis (**h–i**). See also **Extended Data Fig. 5**.

Extended Data Fig. 1

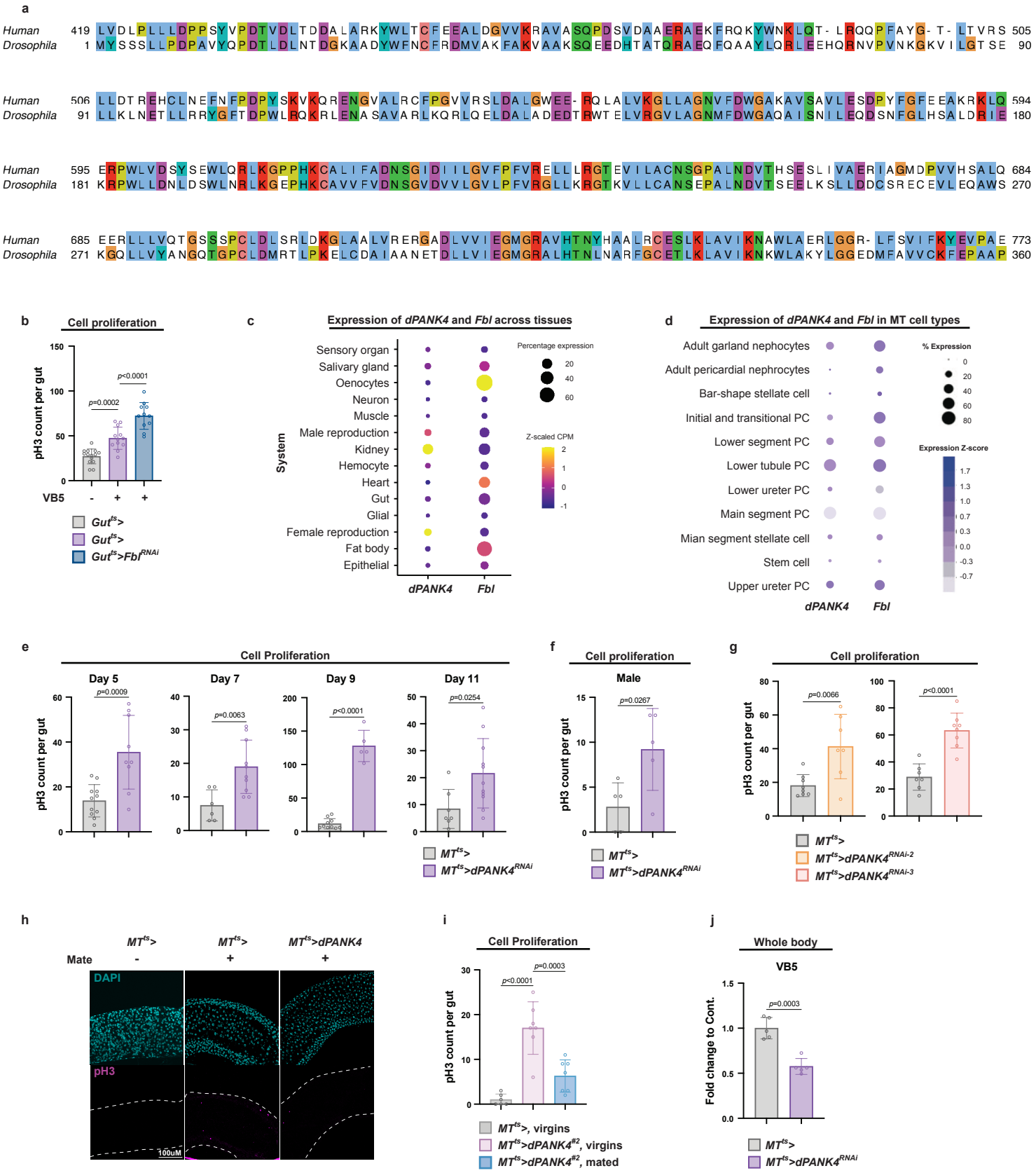

Extended Data Fig. 1 | Related to Figure 2. a, Full length amino acid alignment between human PANK4 and *Drosophila* CG5828 (dPANK4). **b,** Quantification of $pH3^+$ cells per midgut in control versus gut-specific *Fbl* knockdown flies under VB5 supplementation. n = 12-15. **c,** Expression patterns of *dPANK4* and *Fbl* across tissues based on percentage of expressing cells and Z-scaled counts per million (CPM); data from FlyAtlas single-nucleus RNA-seq (snRNA-seq) database. **d,** Expression of *dPANK4* and *Fbl* in cell types of the MTs, represented by percent-expressing cells and Z-scored expression; data from published MT snRNA-seq dataset. PC, principal cell. **e,** Quantification of $pH3^+$ cells per midgut at day 5, 7, 9, and 11 in control and MT-specific *dPANK4* knockdown flies. n = 6-12. **f,** $pH3^+$ cell counts in midguts from male flies with or without MT-specific *dPANK4* knockdown at day 10. n = 5. **g,** $pH3^+$ cell counts in midguts of flies with or without MT-specific dPANK4 *knockdown* at day 10 using two additional independent RNAi lines. n = 8. **h,** Representative gut images from virgin and mated female flies with or without MT-specific *dPANK4* overexpression at day 7. **i,** Quantification of $pH3^+$ cells per midgut from virgin and mated female flies with or without MT-specific *dPANK4* overexpression at day 7 using an independent *dPANK4* overexpression line. n = 6-9. **j,** Relative metabolite levels of VB5 and dephospho-CoA in control and MT-specific *dPANK4* knockdown flies at day 9, retrieved from whole-body metabolomics analysis. n = 5. Statistical significance assessed by unpaired two-sided Student's *t*-test (**e, f, g, j**) and one-way ANOVA (**b, i)**. Error bars indicate s.d., with means at the center.

Extended Data Fig. 2

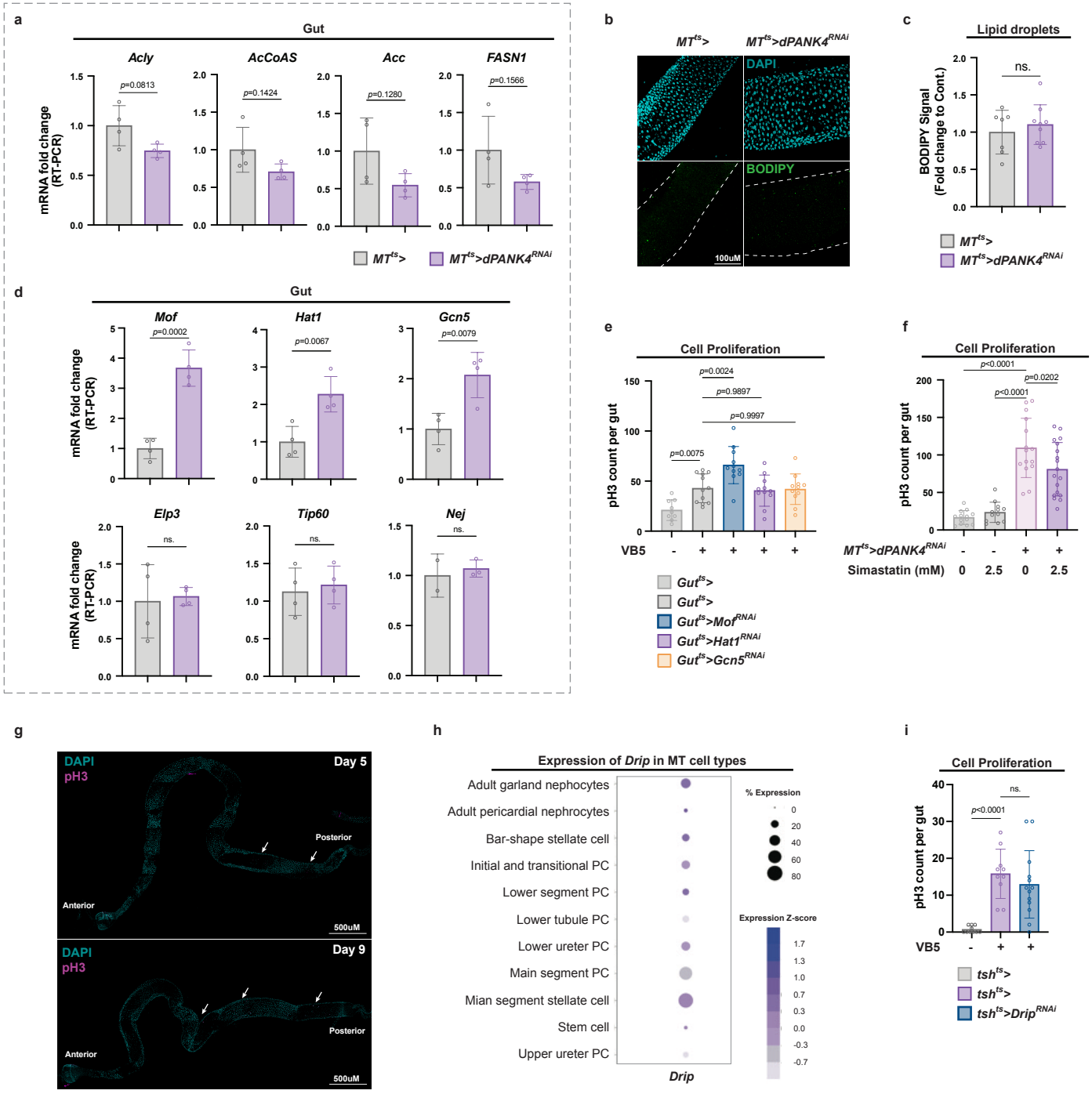

Extended Data Fig. 2 | Related to Figure 3. a, qRT-PCR analysis of lipogenic genes (*Acly, AcCoAS, Acc,* and *FASN1*) mRNA levels in guts from control and MT-specific *dPANK4* knockdown flies at day 9. n = 4. Acly, ATP citrate lyase, ortholog of ATPCL; AcCoAS, acetyl-CoA synthetase, ortholog of ACSS1/2; ACC, acetyl-CoA carboxylase; FASN1, fatty acid synthase 1. **b, c,** Representative images (**b**) and quantification (**c**) of BODIPY lipid staining in guts from control and MT *dPANK4* knockdown flies at day 9. n = 8. **d,** qRT-PCR analysis of histone acetyltransferase genes (*Mof, HAT1, Gcn5, Elp3, Tip60,* and *Nej*) mRNA levels in guts from control and MT *dPANK4* knockdown flies at day 9. n = 4. Nej, ortholog of CBP/p300. **e,** Quantification of pH3+ cells per midgut in flies with gut-specific knockdown of *HAT1, Mof,* or *Gcn5* under VB5 supplementation. **f,** Quantification of $pH3^+$ cells per midgut in flies with or without MT-specific *dPANK4* knockdown at day 10. Flies were fed on control or simvastatin-containing diet for 5 days. n = 10-12. **g,** Representative whole midgut images from control and MT *dPANK4* knockdown flies at day 5 and day 9 showing posterior-biased pH3 signal at day 5 and anterior progression by day 9. **h,** Expression profile of *Drip* in MT cell types, shown as percent of expressing cells and Z-scored expression; data from published MT snRNA-seq dataset. **i,** Quantification of $pH3^+$ cells per midgut in control flies and flies with *Drip* knockdown in stellate cells (*tsh*>) under VB5 supplementation. n = 10-12. Statistical significance assessed by unpaired two-sided Student's *t*-test (**a, c, d**) and one-way ANOVA (**e, f, i)**. Error bars indicate s.d., with means at the center.

Extended Data Fig 3

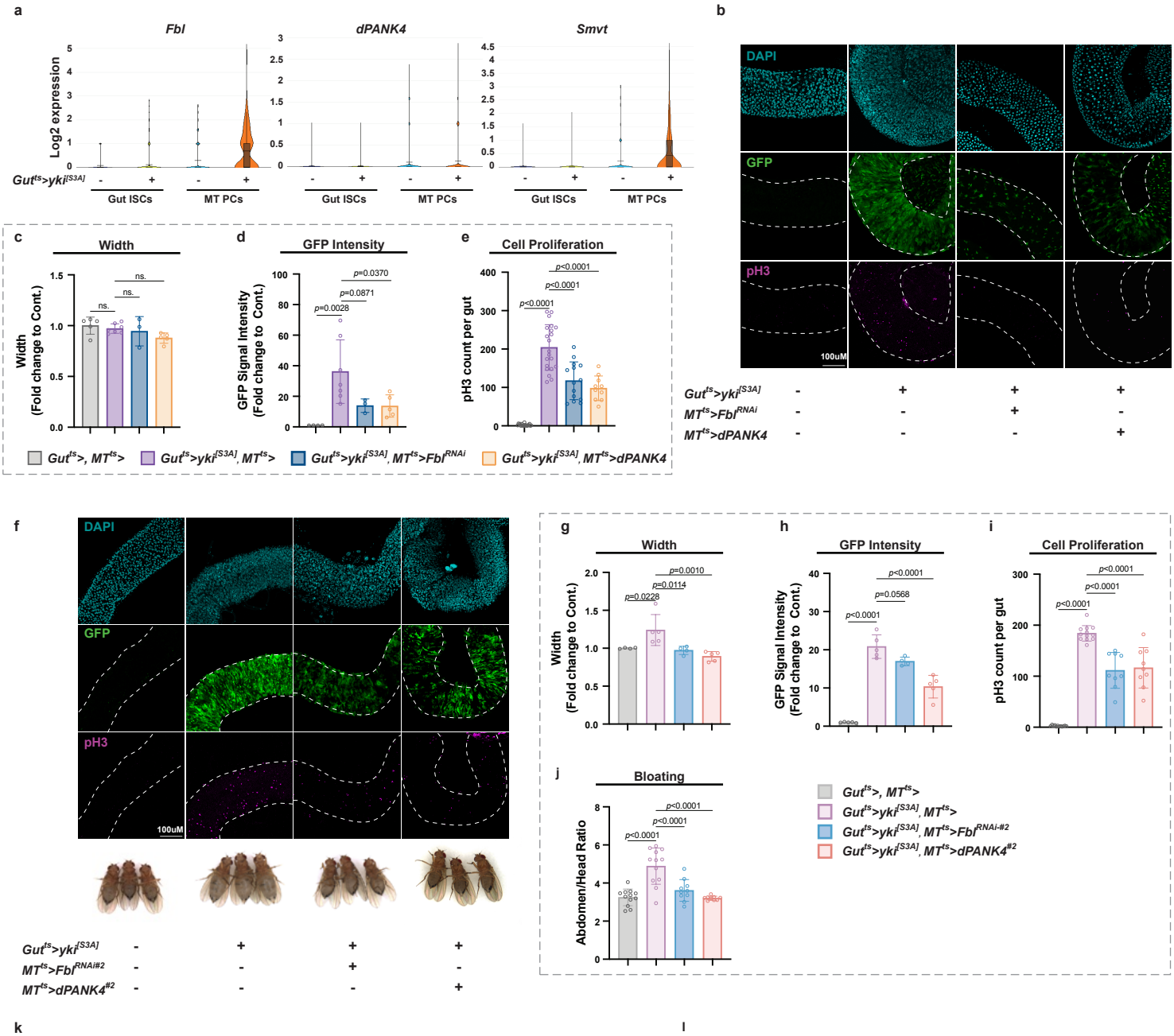

Extended Data Fig. 3 | Related to Figure 4. a, Log2 expression of *dPANK4*, *Fbl*, and *Smvt* in gut ISCs and MT PCs of control and Yki flies; data from published Yki snRNA-seq dataset. **b,** Representative images of guts from control flies and Yki flies with or without MT-specific *Fbl* knockdown or *dPANK4* overexpression at day 3. **c–e,** Quantification of gut width (**c**), GFP intensity (**d**), and $pH3^+$ cell counts (**e**). n = 6-12 **f,** Representative images of guts and representative images of phenotypes from control flies and Yki flies with or without MT-specific *Fbl* knockdown or *dPANK4* overexpression at day 5 using independent fly lines. **g-i,** Quantification of gut width (**g**), GFP intensity (**h**), and $pH3^+$ cell counts (**i**). n = 6-12. **j,** Bloating quantification via abdomen-to-head ratio of panel **f**. n = 12. **k,** Pathway enrichment analysis of gut metabolomics profiling of flies with Yki flies versus controls at day 6. The top enriched KEGG pathways are shown, ranked by statistical significance (-log10(*p*-value)) and colored accordingly. Dot size represents pathway value. n = 4. **m,** Representative images of bloating phenotypes in control and Yki flies with or without simvastatin treatment at day 6. Flies were fed on control or simvastatin-containing diet for 6 days. Statistical significance assessed by one-way ANOVA (**c-e, g-j**) and Fisher's exact test (**k**). Error bars indicate s.d., with means at the center.

Extended Data Fig. 4

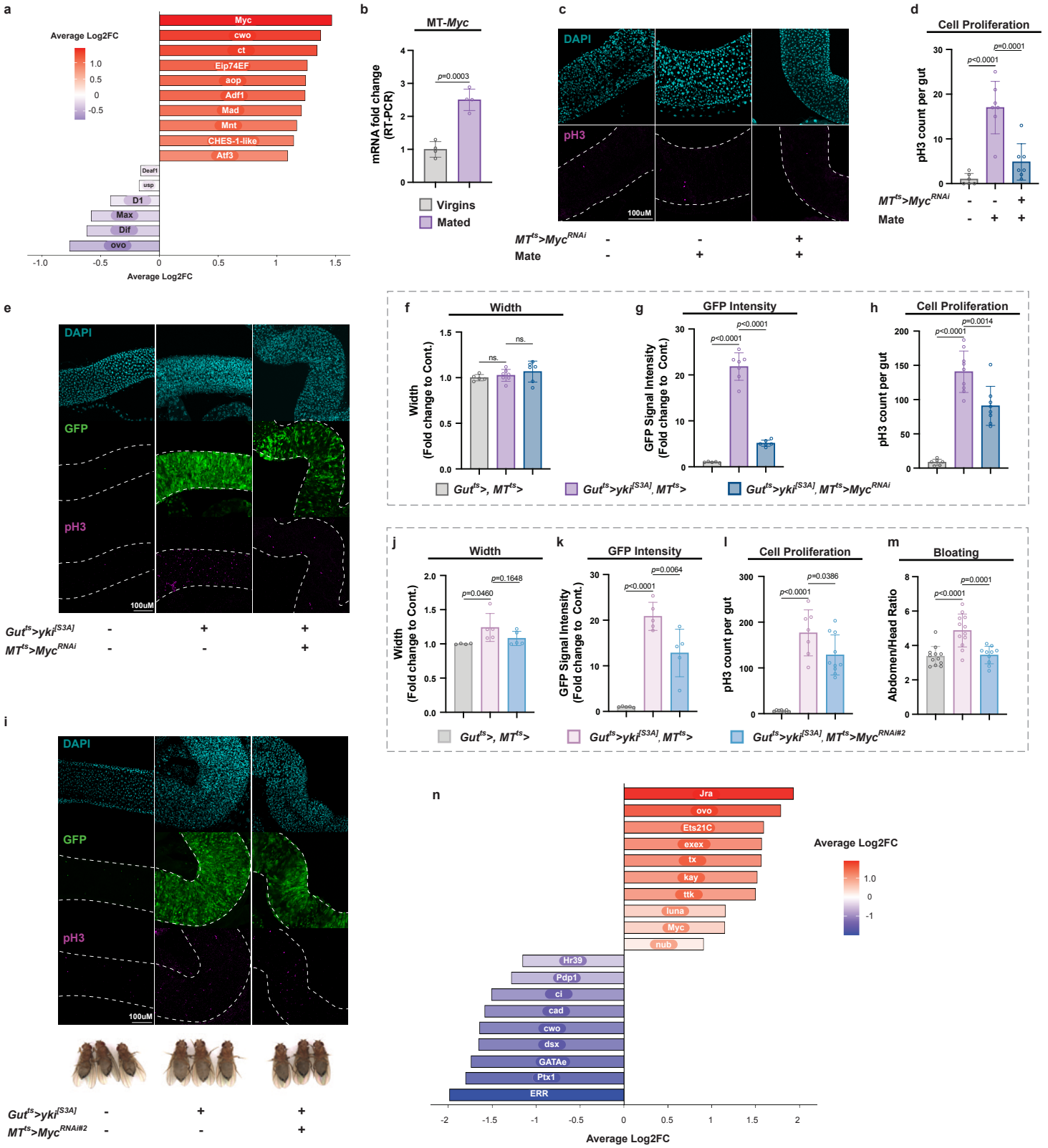

Extended Data Fig. 4 | Related to Figure 5. a, Differential regulon activity analysis of transcription factors in the MTs with published Yki fly snRNA-seq data. A high Log2fc corresponds to increased activity/expression of positively regulated target genes of the regulon in Yki versus control. **b,** qRT-PCR analysis of *Myc* in the MTs of virgin or mated female flies. **c, d,** Representative images (**c**) and quantification (**d**) of pH3+ cells per midgut in virgin or mated female flies with or without MT *Myc* knockdown at day 10. n = 8. **e,** Representative images of guts from control flies and Yki flies with or without MT-specific *Myc* knockdown at day 3. **f-h,** Quantification of gut width (**f**), GFP intensity (**g**), and pH3+ cell counts (**h**). n = 6-8. **i,** Representative images of guts and representative images of phenotypes from control flies and Yki flies with or without MT-specific *Myc* knockdown at day 5 using independent fly lines. **j-l,** Quantification of gut width (**j**), GFP intensity (**k**), and pH3+ cell counts (**l**). n = 6-8. **m,** Bloating quantification via abdomen-to-head ratio from panel **i**. n = 12. **n,** Differential regulon activity analysis of transcription factors in MTs with published snRNA-seq data. A high Log2fc corresponds to increased activity/expression of positively regulated target genes of the regulon in MT-specific Pvr activation versus control. Statistical significance assessed by wilcox test (**a, n**) unpaired two-sided Student's *t*-test (**b**) and one-way ANOVA (**d, f-h, j-m**). Error bars indicate s.d., with means at the center.

Extended Data Fig. 5

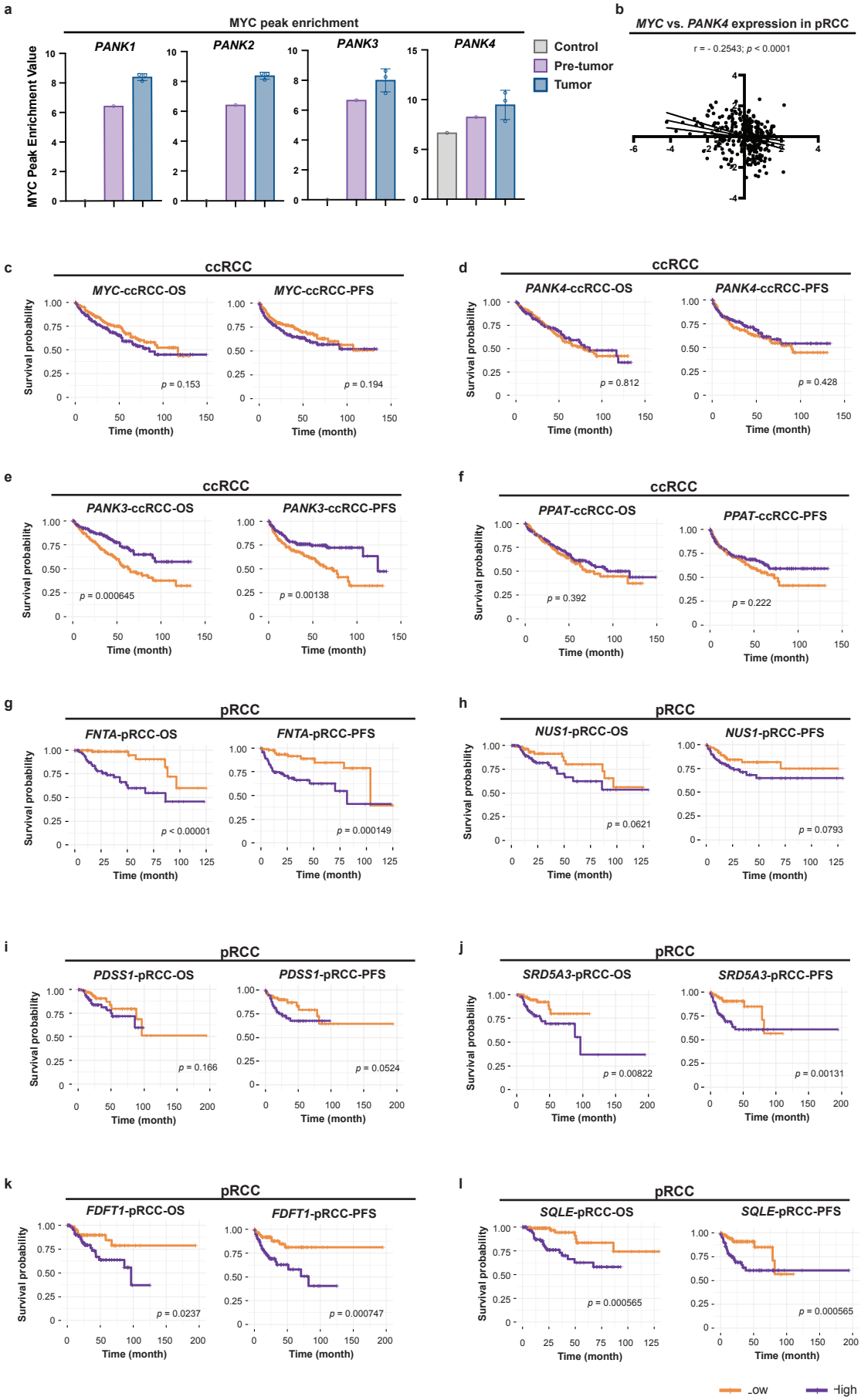

Extended Data Fig. 5

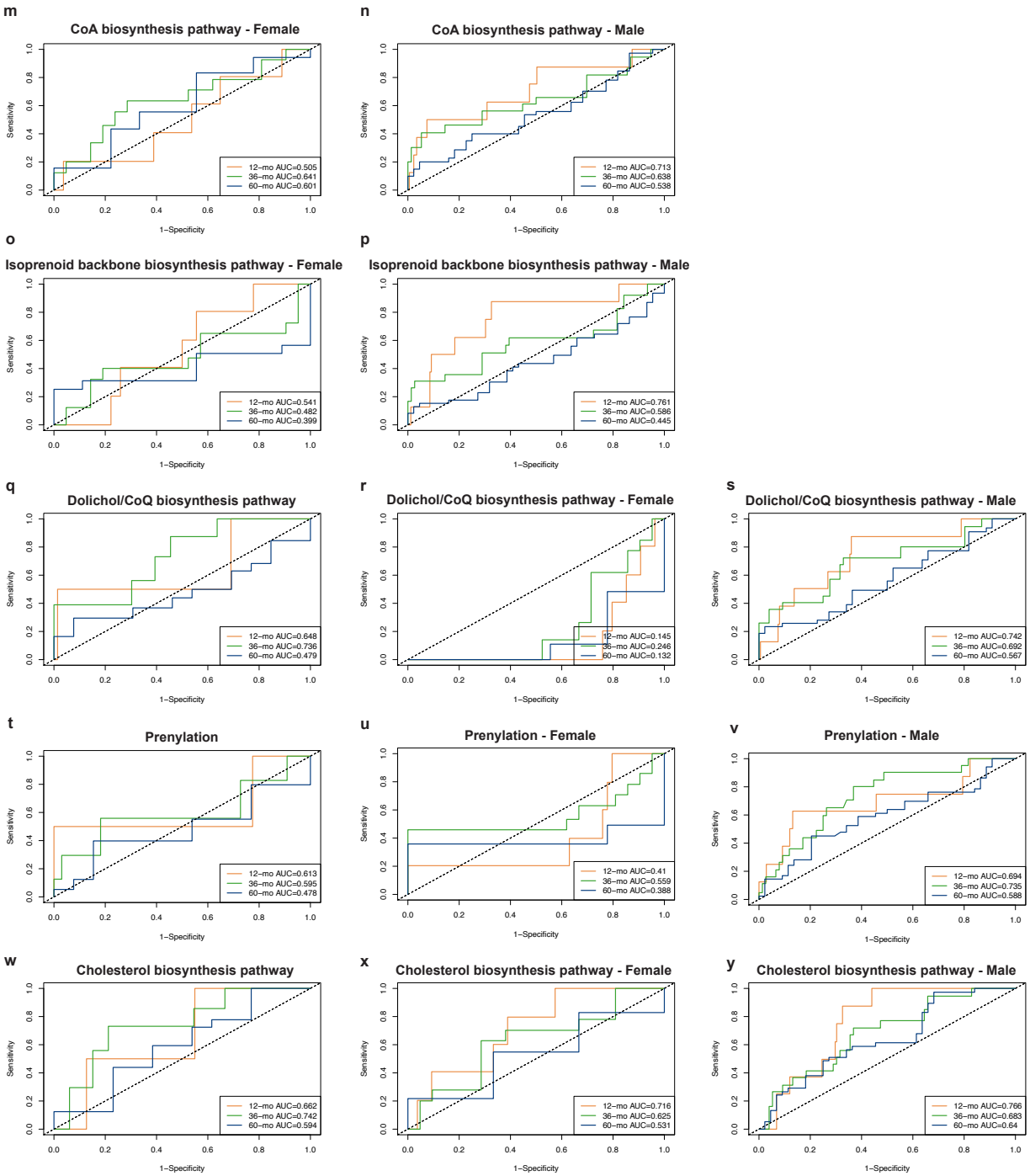

Extended Data Fig. 5 | Related to Figure 6. a, MYC peak enrichment values in the promoter regions of PANK1-4 from published ChIP-seq datasets. Enrichment is calculated as Log2(ChIP - Input), where ChIP and Input represent the number of reads in the peak region normalized by total library size (in millions). A value of 0 is assigned to promoters with no peak called. **b,** Correlation plot showing the negative relationship between MYC and PANK4 expression in 510 Papillary Renal Cell Carcinoma (pRCC/KIRP) patients from the TCGA PanCancer Atlas. **c-f,** Kaplan–Meier (KM) survival analyses of overall survival (OS) and progression-free survival (PFS) in 336 Clear Cell Renal Cell Carcinoma (ccRCC/KIRC) patients comparing low (bottom third) versus high (top third) expression of *MYC* (**c**), *PANK4* (**d**), and *PANK3* (**e**), and *PPAT* (**f**); data from the TCGA PanCancer Atlas. **g-l,** KM survival analyses (OS and PFS) for 188 pRCC patients stratified by expression of *FNTA* (**g**), *NUS1* (**h**), *PDSS1* (**i**), *SRD5A3* (**j**), *FDFT1* (**k**), and *SQLE* (**l**), comparing bottom versus top expression tertiles. **m-p,** Time-dependent ROC (receiver operating characteristic) curve analyses showing AUC (area under the curve) values at 12, 24, and 36 months of metastasis stage M0. Panels **m-n** show AUC for CoA biosynthesis gene signatures in female (**m**) (n = 72) and male (**n**) (n = 208) pRCC patients; panels **o-p** show AUC for isoprenoid backbone biosynthesis gene signatures in female (**o**) (n = 72) and male (**p**) (n = 208) patients. Pathway gene sets include: CoA biosynthesis: *PANK1-4, PPCS, PPCDC, PPAT* and *COASY*; isoprenoid backbone synthesis: *MVK, PMVK, MVD, IDI1, IDI2, FDPS* and *GGPS1*. **q-y,** Time-dependent ROC analysis of dolichol and ubiquinone (CoQ) biosynthesis gene signatures in pRCC patients showing AUC performance across both genders (**q**) (n = 91), females (**r**) (n = 72), and males (**s**) (n = 208). Pathway gene sets include: *DHDDS, NUS1, SRD5A1* and *PDSS1/2*. **t-v,** Time-dependent ROC analysis of protein prenylation gene signatures in pRCC patients showing AUC performance across both genders (**t**) (n = 91), females (**u**) (n = 72), and males (**v**) (n = 208). Pathway gene sets include: *FNTA, FNTB* and *PGGT1B*. **w-y,** Time-dependent ROC analysis of cholesterol biosynthesis gene signatures in pRCC patients showing AUC performance across both genders (**w**) (n = 91), females (**x**) (n = 72), and males (**y**) (n = 208). Pathway gene sets include: *FDFT1, SQLE, LSS, CYP51A1* and *DHCG7*. Statistical significance assessed by Pearson correlation analysis (**b**), log-rank (Mantel-Cox) test for survival curves (**c-l**), and AUC analyses (**m-y**).

References

1. Awuchi, C.G., V.S. Igwe, I. Amagwula, and C.K. Echeta, *Health benefits of micronutrients (vitamins and minerals) and their associated deficiency diseases: A systematic review.* International Journal of Food Sciences, 2020. **3**(1): p. 1-32.
2. Tardy, A.-L., et al., *Vitamins and minerals for energy, fatigue and cognition: a narrative review of the biochemical and clinical evidence.* Nutrients, 2020. **12**(1): p. 228.
3. Schellack, G., P. Harirari, and N. Schellack, *B-complex vitamin deficiency and supplementation.* SA Pharmaceutical Journal, 2016. **83**(4): p. 14-19.
4. Chen, C.-C., et al., *Vitamin B6 addiction in acute myeloid leukemia.* Cancer Cell, 2020. **37**(1): p. 71-84. e7.
5. Barritt, S.A., S.E. DuBois-Coyne, and C.C. Dibble, *Coenzyme A biosynthesis: mechanisms of regulation, function and disease.* Nature Metabolism, 2024. **6**(6): p. 1008-1023.
6. Tahiliani, A.G. and C.J. Beinlich, *Pantothenic acid in health and disease.* Vitamins & Hormones, 1991. **46**: p. 165-228.
7. Leonardi, R., Y.-M. Zhang, C.O. Rock, and S. Jackowski, *Coenzyme A: back in action.* Progress in lipid research, 2005. **44**(2-3): p. 125-153.
8. Czumaj, A., et al., *The pathophysiological role of CoA.* International Journal of Molecular Sciences, 2020. **21**(23): p. 9057.
9. Dibble, C.C., et al., *PI3K drives the de novo synthesis of coenzyme A from vitamin B5.* Nature, 2022. **608**(7921): p. 192-198.
10. Karasawa, T., K. YOSHIDA, K. FURUKAWA, and K. HOSOKI, *Feedback inhibition of pantothenate kinase by coenzyme A and possible role of the enzyme for the regulation of cellular coenzyme A level.* The Journal of Biochemistry, 1972. **71**(6): p. 1065-1067.
11. Subramanian, C., et al., *Allosteric regulation of mammalian pantothenate kinase.* Journal of Biological Chemistry, 2016. **291**(42): p. 22302-22314.
12. Böhlig, L., M. Friedrich, and K. Engeland, *p53 activates the PANK1/miRNA-107 gene leading to downregulation of CDK6 and p130 cell cycle proteins.* Nucleic acids research, 2011. **39**(2): p. 440-453.
13. Wang, S.-J., et al., *p53-Dependent regulation of metabolic function through transcriptional activation of pantothenate kinase-1 gene.* Cell cycle, 2013. **12**(5): p. 753-761.
14. Sabo, A., et al., *Selective transcriptional regulation by Myc in cellular growth control and lymphomagenesis.* Nature, 2014. **511**(7510): p. 488-492.
15. Kreuzaler, P., et al., *Vitamin B5 supports MYC oncogenic metabolism and tumor progression in breast cancer.* Nature metabolism, 2023. **5**(11): p. 1870-1886.
16. Jeon, Y.G., Y.Y. Kim, G. Lee, and J.B. Kim, *Physiological and pathological roles of lipogenesis.* Nature Metabolism, 2023. **5**(5): p. 735-759.
17. Miziorko, H.M., *Enzymes of the mevalonate pathway of isoprenoid biosynthesis.* Archives of biochemistry and biophysics, 2011. **505**(2): p. 131-143.
18. Miao, T., et al., *Acetyl-CoA-mediated autoacetylation of fatty acid synthase as a metabolic switch of de novo lipogenesis in Drosophila.* Proceedings of the National Academy of Sciences, 2022. **119**(49): p. e2212220119.
19. Clendening, J.W., et al., *Dysregulation of the mevalonate pathway promotes transformation.* Proceedings of the National Academy of Sciences, 2010. **107**(34): p. 15051-15056.
20. Wong, W.W.-L., et al., *Determinants of sensitivity to lovastatin-induced apoptosis in multiple myeloma.* Molecular cancer therapeutics, 2007. **6**(6): p. 1886-1897.

21. Clendening, J.W., et al., *Exploiting the mevalonate pathway to distinguish statin-sensitive multiple myeloma.* Blood, The Journal of the American Society of Hematology, 2010. **115**(23): p. 4787-4797.
22. Mullen, P.J., et al., *The interplay between cell signalling and the mevalonate pathway in cancer.* Nature Reviews Cancer, 2016. **16**(11): p. 718-731.
23. Singh, P., et al., *Cholesterol biosynthesis and homeostasis in regulation of the cell cycle.* PloS one, 2013. **8**(3): p. e58833.
24. Zhu, Y., P.J. Casey, A.P. Kumar, and S. Pervaiz, *Deciphering the signaling networks underlying simvastatin-induced apoptosis in human cancer cells: evidence for non-canonical activation of RhoA and Rac1 GTPases.* Cell death & disease, 2013. **4**(4): p. e568-e568.
25. Freed-Pastor, W.A., et al., *Mutant p53 disrupts mammary tissue architecture via the mevalonate pathway.* Cell, 2012. **148**(1): p. 244-258.
26. Snaebjornsson, M.T., S. Janaki-Raman, and A. Schulze, *Greasing the wheels of the cancer machine: the role of lipid metabolism in cancer.* Cell metabolism, 2020. **31**(1): p. 62-76.
27. Rajan, A. and J. Karpac, *Inter-organ communication in Drosophila: Lipoproteins, adipokines, and immune-metabolic coordination.* Current Opinion in Cell Biology, 2025. **94**: p. 102508.
28. Droujinine, I.A. and N. Perrimon, *Interorgan communication pathways in physiology: focus on Drosophila.* Annual review of genetics, 2016. **50**(1): p. 539-570.
29. Kwon, Y., et al., *Systemic Organ Wasting Induced by Localized Expression of the Secreted Insulin/IGF Antagonist ImpL2.* Developmental Cell, 2015. **33**(1): p. 36-46.
30. Micchelli, C.A. and N. Perrimon, *Evidence that stem cells reside in the adult Drosophila midgut epithelium.* Nature, 2006. **439**(7075): p. 475-479.
31. Ohlstein, B. and A. Spradling, *The adult Drosophila posterior midgut is maintained by pluripotent stem cells.* Nature, 2006. **439**(7075): p. 470-474.
32. Ohlstein, B. and A. Spradling, *Multipotent Drosophila intestinal stem cells specify daughter cell fates by differential notch signaling.* Science, 2007. **315**(5814): p. 988-992.
33. Afshar, K., P. Gönczy, S. DiNardo, and S.A. Wasserman, *fumble encodes a pantothenate kinase homolog required for proper mitosis and meiosis in Drosophila melanogaster.* Genetics, 2001. **157**(3): p. 1267-1276.
34. Li, H., et al., *Fly Cell Atlas: A single-nucleus transcriptomic atlas of the adult fruit fly.* Science, 2022. **375**(6584): p. eabk2432.
35. Xu, J., et al., *Transcriptional and functional motifs defining renal function revealed by single-nucleus RNA sequencing.* Proceedings of the National Academy of Sciences, 2022. **119**(25).
36. Xu, J., et al., *Mechanistic characterization of a Drosophila model of paraneoplastic nephrotic syndrome.* Nature Communications, 2024. **15**(1).
37. Ahmed, S.M.H., et al., *Fitness trade-offs incurred by ovary-to-gut steroid signalling in Drosophila.* Nature, 2020. **584**(7821): p. 415-419.
38. Zipper, L., et al., *Ecdysone steroid hormone remote controls intestinal stem cell fate decisions via the PPARγ-homolog Eip75B in Drosophila.* elife, 2020. **9**: p. e55795.
39. Menzies, K.J., H. Zhang, E. Katsyuba, and J. Auwerx, *Protein acetylation in metabolism—metabolites and cofactors.* Nature Reviews Endocrinology, 2016. **12**(1): p. 43.
40. Sheikh, B.N. and A. Akhtar, *The many lives of KATs — detectors, integrators and modulators of the cellular environment.* Nature Reviews Genetics, 2019. **20**(1): p. 7-23.
41. Larsson, O., *HMG-CoA reductase inhibitors: role in normal and malignant cells.* Critical reviews in oncology/hematology, 1996. **22**(3): p. 197-212.

42. Bellés, X., D. Martín, and M.-D. Piulachs, *The mevalonate pathway and the synthesis of juvenile hormone in insects.* Annu. Rev. Entomol., 2005. **50**(1): p. 181-199.
43. Sorrentino, G., et al., *Metabolic control of YAP and TAZ by the mevalonate pathway.* Nature cell biology, 2014. **16**(4): p. 357-366.
44. Liu, Z., H. Zhang, B. Lemaitre, and X. Li, *Duox activation in Drosophila Malpighian tubules stimulates intestinal epithelial renewal through a countercurrent flow.* Cell Reports, 2024. **43**(4).
45. Cabrero, P., et al., *Specialized stellate cells offer a privileged route for rapid water flux in Drosophila renal tubule.* Proceedings of the National Academy of Sciences, 2020. **117**(3): p. 1779-1787.
46. Liu, Y., et al., *Hepatic gluconeogenesis and PDK3 upregulation drive cancer cachexia in flies and mice.* Nature Metabolism, 2025. **7**(4): p. 823-841.
47. Hu, Y., et al., *TF2TG: an online resource mining the potential gene targets of transcription factors in Drosophila.* Genetics, 2025: p. iyaf082.
48. Ding, G., et al., *Coordination of tumor growth and host wasting by tumor-derived Upd3.* Cell Reports, 2021. **36**(7): p. 109553.
49. Song, W., et al., *Tumor-Derived Ligands Trigger Tumor Growth and Host Wasting via Differential MEK Activation.* Developmental Cell, 2019. **48**(2): p. 277-286.e6.
50. Chiariello, M., M.J. Marinissen, and J.S. Gutkind, *Regulation of c-myc expression by PDGF through Rho GTPases.* Nature cell biology, 2001. **3**(6): p. 580-586.
51. Xu, J., et al., *Mechanistic characterization of a Drosophila model of paraneoplastic nephrotic syndrome.* Nature Communications, 2024. **15**(1): p. 1241.
52. Sabò, A., et al., *Selective transcriptional regulation by Myc in cellular growth control and lymphomagenesis.* Nature, 2014. **511**(7510): p. 488-492.
53. Lorraine, et al., *Physiological roles of the pantothenate kinases.* Biochemical Society Transactions, 2014. **42**(4): p. 1033-1036.
54. Duff, M.O., et al., *Genome-wide identification of zero nucleotide recursive splicing in Drosophila.* Nature, 2015. **521**(7552): p. 376-379.
55. Hsieh, J.J., et al., *Renal cell carcinoma.* Nature reviews Disease primers, 2017. **3**(1): p. 1-19.
56. Liu, J., et al., *An integrated TCGA pan-cancer clinical data resource to drive high-quality survival outcome analytics.* Cell, 2018. **173**(2): p. 400-416. e11.
57. Hoadley, K.A., et al., *Cell-of-origin patterns dominate the molecular classification of 10,000 tumors from 33 types of cancer.* Cell, 2018. **173**(2): p. 291-304. e6.
58. Leonardi, R., J.E. Rehg, C.O. Rock, and S. Jackowski, *Pantothenate kinase 1 is required to support the metabolic transition from the fed to the fasted state.* PloS one, 2010. **5**(6): p. e11107.
59. Yu, Y., et al., *Coenzyme A precursors flow from mother to zygote and from microbiome to host.* Molecular Cell, 2022. **82**(14): p. 2650-2665.e12.
60. Srinivasan, B., et al., *Extracellular 4'-phosphopantetheine is a source for intracellular coenzyme A synthesis.* Nature chemical biology, 2015. **11**(10): p. 784-792.
61. Ma, Y., et al., *Fatty acid metabolism and acyl-CoA synthetases in the liver-gut axis.* World Journal of Hepatology, 2021. **13**(11): p. 1512.
62. Varghese, A., et al., *Unravelling cysteine-deficiency-associated rapid weight loss.* Nature, 2025.
63. Wang, C., et al., *Alternative approaches to target Myc for cancer treatment.* Signal Transduction and Targeted Therapy, 2021. **6**(1): p. 117.
64. Whitfield, J.R. and L. Soucek, *MYC in cancer: from undruggable target to clinical trials.* Nature Reviews Drug Discovery, 2025: p. 1-13.
65. Staller, P., et al., *Repression of p15INK4b expression by Myc through association with Miz-1.* Nature cell biology, 2001. **3**(4): p. 392-399.

66. Zhao, D., et al., *VEGF drives cancer-initiating stem cells through VEGFR-2/Stat3 signaling to upregulate Myc and Sox2.* Oncogene, 2015. **34**(24): p. 3107-3119.
67. Mendoza, M.C., E.E. Er, and J. Blenis, *The Ras-ERK and PI3K-mTOR pathways: cross-talk and compensation.* Trends in biochemical sciences, 2011. **36**(6): p. 320-328.
68. Shibuya, M., *Vascular endothelial growth factor (VEGF) and its receptor (VEGFR) signaling in angiogenesis: a crucial target for anti-and pro-angiogenic therapies.* Genes & cancer, 2011. **2**(12): p. 1097-1105.
69. Jiménez-Valerio, G. and O. Casanovas, *Angiogenesis and metabolism: entwined for therapy resistance.* Trends in Cancer, 2017. **3**(1): p. 10-18.
70. Ricketts, C.J., et al., *The cancer genome atlas comprehensive molecular characterization of renal cell carcinoma.* Cell reports, 2018. **23**(1): p. 313-326. e5.
71. Pal, S.K., et al., *A comparison of sunitinib with cabozantinib, crizotinib, and savolitinib for treatment of advanced papillary renal cell carcinoma: a randomised, open-label, phase 2 trial.* The Lancet, 2021. **397**(10275): p. 695-703.
72. Mendhiratta, N., P. Muraki, A.E. Sisk Jr, and B. Shuch. *Papillary renal cell carcinoma*. in *Urologic Oncology: Seminars and Original Investigations*. 2021. Elsevier.
73. Raiteri, M., et al., *Pharmacological control of the mevalonate pathway: effect on arterial smooth muscle cell proliferation.* The Journal of pharmacology and experimental therapeutics, 1997. **281**(3): p. 1144-1153.
74. Shellman, Y.G., et al., *Lovastatin-induced apoptosis in human melanoma cell lines.* Melanoma research, 2005. **15**(2): p. 83-89.
75. Lee, W.-C. and C.A. Micchelli, *Development and characterization of a chemically defined food for Drosophila.* PloS one, 2013. **8**(7): p. e67308.
76. Piper, M.D., et al., *A holidic medium for Drosophila melanogaster.* Nature methods, 2014. **11**(1): p. 100-105.
77. Troen, A.M., et al., *Lifespan modification by glucose and methionine in Drosophila melanogaster fed a chemically defined diet.* Age, 2007. **29**(1): p. 29-39.
78. Oh, H. and K.D. Irvine, *In vivo analysis of Yorkie phosphorylation sites.* Oncogene, 2009. **28**(17): p. 1916-1927.
79. Saavedra, P., et al., *REPTOR and CREBRF encode key regulators of muscle energy metabolism.* Nature Communications, 2023. **14**(1): p. 4943.